This manuscript is a preprint and has been submitted for publication in **ISPRS Journal of Photogrammetry and Remote Sensing**. Please note that, despite ongoing peer-review, the manuscript has yet to be formally accepted for publication. Subsequent versions of this manuscript may have slightly different content. If accepted, the final version of this manuscript will be available via the 'peer-reviewed Publication DOI' link on the right-hand side of this webpage. Please feel free to contact any of the authors; we welcome feedback.

Developing seagrass index for long term monitoring of *Zostera japonica* seagrass bed: a case study in Yellow River Delta, China

Qingqing Zhou[a], Yinghai Ke[a*], Xinyan Wang[b], Junhong Bai[b], Demin Zhou[a,b,c], Xiaojuan Li[a,b,c*]

[a] Beijing Laboratory of Water Resources Security, Capital Normal University, Beijing, 100048, China

[b] State Key Laboratory of Water Environment Simulation, Beijing Normal University, Beijing 100875, China

[c] College of Geospatial Information Science and Technology, Capital Normal University, Beijing, 100048, China;

[d] College of Resource Environment and Tourism, Capital Normal University, Beijing, 100048, China;

Corresponding Author: Yinghai Ke, Ph. D, yke@cnu.edu.cn;

Xiaojuan Li, Ph. D, lixiaojuan@cnu.edu.cn

Developing seagrass index for long term monitoring of *Zostera japonica* seagrass bed: a case study in Yellow River Delta, China

Abstract

Seagrass beds offer unique and vital ecological services as an important blue carbon ecosystem in coastal wetlands. *Zostera japonica* is an intertidal seagrass species native to eastern Asia and is one of the most widely distributed seagrass species in China. However, little is known on the long-term variations of *Z. japonica* extents. Automatic mapping method for *Z. japonica* seagrass beds is in urgent need to fill this knowledge gap. In this study, we proposed a new SeaGrass Index (SGI) for automatic and rapid mapping of *Z. japonica* based on time-series Landsat satellite imagery, aiming to alleviate the influence of tidal inundation and enhance the separability from other coastal cover types. The SGI considers both spectral and phenological characteristics of *Z. japonica*, as well as the spatial location of *Z. japonica*. We took the Yellow River Delta (YRD), China as our study area, where *Z. japonica* was first discovered and reported in 2015. Based on SGI, *Z. japonica* extents during 1985-2018 were extracted using multi-Otsu thresholding algorithm. Accuracy assessments based on field investigations and high-resolution imagery showed that SGI has successfully separated seagrass beds from other cover types, especially intertidal salt marshes, with overall accuracies >95%, producer's accuracies >90% and user's accuracies >94%. Our study provides the first long-term maps of seagrass beds in YRD. The area of *Z. japonica* showed large variations during 1985-2018, ranging from 149 ha in 2005-2006 to 1302.9 ha in 2011-2012. The spatial distribution of *Z.*

japonica varied with the morphological change of the estuary caused by river channel shifts. Since 2011, *Z. japonica* seagrass beds have undergone area degradation due to the invasion of *S. alterniflora*. The area was only 332.3 ha in 2017-2018. Coastal erosion and extreme climate events such as drought and typhoon might also explain degradation of seagrass beds in YRD. We expect that the SGI will advance automatic and rapid mapping methods for intertidal seagrass beds, and the *Z. japonica* maps will provide a baseline data for restoration and management of seagrasses at regional scale.

Keywords: Seagrass mapping; Zostera japonica; Time-series analysis; Multi-Otsu algorithm; Yellow River Delta

1 Introduction

Seagrasses are marine plants found in shallow coastal and estuarine waters in many parts of the world from the equator to high latitude except Antarctica. Seagrass beds are one of the most valuable marine and coastal ecosystems in the world (Programme, 2020). They form important nursery habitats and support coastal food webs for thousands of marine species (Iacarella et al., 2018). In addition, they provide significant services including sediment stabilization, coastal erosion reduction, water purification and nutrient cycling (Programme, 2020; Green et al., 2021). Meanwhile, seagrass beds are important blue carbon ecosystems. Although seagrass beds cover less than 0.2% of the total ocean area, they store approximately 10% to 20% of the global marine carbon (Fourqurean et al., 2012; Campbell et al., 2022). They also bring valuable socio-economic benefits by providing food and livelihoods for coastal communities.

Unfortunately, seagrass beds are one of the most threatened marine ecosystems. Researches have shown that 29% of the known seagrass beds have disappeared since first recorded in 1879, and the global seagrass beds are being lost at a rate of 1.5% per year (Green et al., 2021). Global climate change, including the elevated seawater temperature and the increasingly extreme weather events such as hurricanes and ocean heat waves, has caused serious damage to seagrass beds (Yue et al., 2021). Human activities such as beach aquaculture, coastal development and water pollution also pose threats to seagrass beds, resulting in habitat fragmentation and degradation, presenting negative feedback to coastal ecosystem and climate change (Adams et al., 2016; Salinas et al., 2020).

Zostera japonica (also called dwarf eelgrass or Japanese eelgrass) is a seagrass species native to eastern Asia from Vietnam to Russia. It is one of the most widely distributed seagrass species in China's coastal areas and can be found primarily in intertidal zones. The Yellow River Delta (YRD) is the youngest and broadest coastal wetland ecosystem in China (Li et al., 2019). In 2015, researchers discovered a large *Z. japonica* meadow in the intertidal zone of YRD during field investigations, which was the first record of the seagrass distribution in YRD (Zhou et al., 2016). However, to date little is known about the spatial and temporal dynamics of *Z. japonica* extents in YRD during the past decades. In recent years, YRD has experienced dramatic morphological and landscape changes due to river channel shifts, coastline variations and rapid expansion of invasive plant species *Spartina Alterniflora* (Li et al., 2019; Wang et al., 2021; Li et al., 2021). In this highly dynamic area, *Z. japonica* mapping and monitoring over the past decades are vital for better understating their responses to climate change and human activities, and for sustainable management and conservation of the coastal wetlands.

Compared to in-situ field investigations and acoustic-based techniques, satellite remote sensing techniques provide unique opportunities for seagrass monitoring over large area in an efficient and cost-effective manner (Hossain et al., 2015a; Programme, 2020; Veettil et al., 2020; Li et al., 2021). As reviewed by Hossain et al. (2015) and Veettil et al., (2020), seagrass mapping approaches should consider habitat conditions including water depth (exposed intertidal, submerged intertidal, shallow subtidal or deep subtidal) and water clarity (clear or turbid). For submerged seagrasses in subtidal area (e.g., water depth > 2 m), water depth corrections are usually required to reduce the effects of water attenuation and retrieve bottom reflectance, based on which seagrasses are identified (Kuhwald et al., 2021; Tu et al., 2021). For intertidal seagrasses which are exposed during low tide, surface reflectance-based vegetation indices, such as Normalized Differential Vegetation Index (NDVI) have been adopted to delineate seagrass extents (Valle et al., 2015; Zoffoli et al., 2020; Zoffoli et al., 2021).

At present, multispectral satellite data with spatial resolutions from hundreds of meters to sub-meter including MODIS, Landsat series, Sentinel-2, SPOT series, QuickBird, WorldView-2/3 and PlanetScope have been used for seagrass mapping in different coastal areas (Hossain et al., 2015b; Veettil et al., 2020). For intertidal seagrasses such as *Zostera noltei* or *Zostera marina*, some researchers have investigated monitoring long-term variations of seagrass extents based on satellite imagery acquired on multiple years (Calleja et al., 2017; Zoffoli et al., 2020; Zoffoli et al., 2021). These studies generally selected single-date cloud-clear image acquired at low tide and identified seagrasses using supervised classification (Coffer et al., 2020; Kuhwald et al., 2021; Carpenter et al., 2022; Lebrasse et al., 2022) or unsupervised classification (Barrell and Grant, 2015; St-Pierre and Gagnon, 2020; Xu et al., 2021). For example, Calleja et al. (2017) selected 10 cloudless Landsat images with lowest tidal level for each summer during 1984-2015 and developed rule-based thresholds to identify *Zostera noltei* in Bay of Santander, Spain. Xu et al. (2021) selected low-tide Landsat images from 1974 to 2019 and used ISODATA clustering algorithm to map *Zostera marina* seagrasses in Caofeidian, Bohai Sea, China. Fernandes et al. (2022) selected 21 cloud-free and low-turbidity Landsat images acquired during summer from 1988 to 2018 and utilized Support Vector Machine to separate seagrasses from sand in Adelaide, South Australia.

However, uncertainties exist when using single-date images for long-term mapping of seagrasses. First, in coastal areas with frequent cloud coverage and tidal inundation, it is difficult to find an adequate image acquired in the growing season that is neither contaminated by cloud nor influenced by tide level. Second, when seagrasses and other coastal vegetation (e.g., intertidal salt marshes such as *S. alterniflora* in YRD) are mixed, it is difficult to discriminate them because they may have similar spectral features during growing seasons. When it comes to the YRD, additional challenge exists due to the high turbidity of coastal water. The Yellow River estuary is one of the most turbid estuaries in the world, with high concentration of suspended particulate matter in the coastal water (Li et al., 2019). The sediments may cover the seagrasses even during low tide and make it more difficult for discrimination. Furthermore, supervised classifications that have been used for seagrass mapping or coastal land cover classification in many studies are challenging for long-term time-series seagrass mapping due to lack of field data for training sample collection for the retrospective analysis.

To address these issues, this study aims to: (1) present a SeaGrass Index (SGI) that is capable of discriminating *Z. japonica* from other coastal cover types and alleviating the influence of frequent cloud cover and tidal inundation, (2) develop an unsupervised classification approach for automatic extraction of *Z. japonica* in YRD based on SGI. Both SGI and the classification approach are to be developed on Google Earth Engine (GEE) platform to facilitate rapid mapping of *Z. japonica* extent, and (3) investigate long-term spatial and temporal variations of *Z. japonica* distribution during 1985-2018 in YRD.

2 Study area and data

2.1 Study area

The YRD is located in Shandong Province, China, adjacent to the Bohai Sea in the north and Laizhou Bay in the east. It belongs to temperate continental monsoon climate, with an average annual temperature of 11.5-12.9 °C and average annual precipitation of 592.2 mm. Precipitation is mostly concentrated in July and August. The Yellow River estuary has weak tides, with an average tidal range of 0.73-1.77 m, and is dominated by irregular semi-diurnal tide pattern (Yang et al., 2011). Our study area is located in the Yellow River Delta National Natural Reserve with an area of 1530 km^2 (Fig. 1). *Z. japonica* meadows are distributed in the lower intertidal area which are submerged at high tide and exposed to air for 4-8 hours at low tide. The growing season is from June to August (Liu et al., 2019; Zhang et al., 2019). The native salt marsh vegetations include *S. alterniflora*, *Saueda salsa*, *Tamarix chinensis*, and

Phragmites australis. *S. alterniflora* is an invasive species in YRD. It was first found in the intertidal zones in 2008 and since then it has expanded rapidly (Wang et al., 2021). In recent years, it was reported that *S. alterniflora* started to encroached ecological niches of *Z. japonica* (Ren et al., 2019; Ma et al., 2020). *S. salsa* grows on both mid-high intertidal area and low intertidal area near the coastline. *T. chinensis* and *P. australis* grow in high-tide area. The study area is featured considerable sediment deposition because Yellow River carries an average 1.0 billion tons of sediment per year. The river channel in the delta has shifted many times in history. During the past fifty years, it was artificially shifted from the Diaokou course to the Qingshuigou course in 1976 (Fig. 1a), and then to Q8 in 1996 (Fig. 1b). In 2007, the downstream end of the Q8 course shifted naturally because of the change in riverine dynamics (Fan et al., 2018; Li et al., 2019). As a results, the shape of the coastline in the estuary has changed dramatically during the past a few decades. Based on the locations of river course channels during the study period, we divided the study area into three zones, namely Zone A, B and C (Fig. 1). Zone A covers the north bank of YRD after the river course shifted in 2007. Zone C covers the south bank of YRD before the river course shifted in 1996. Zone B is located between Zone A and Zone C.

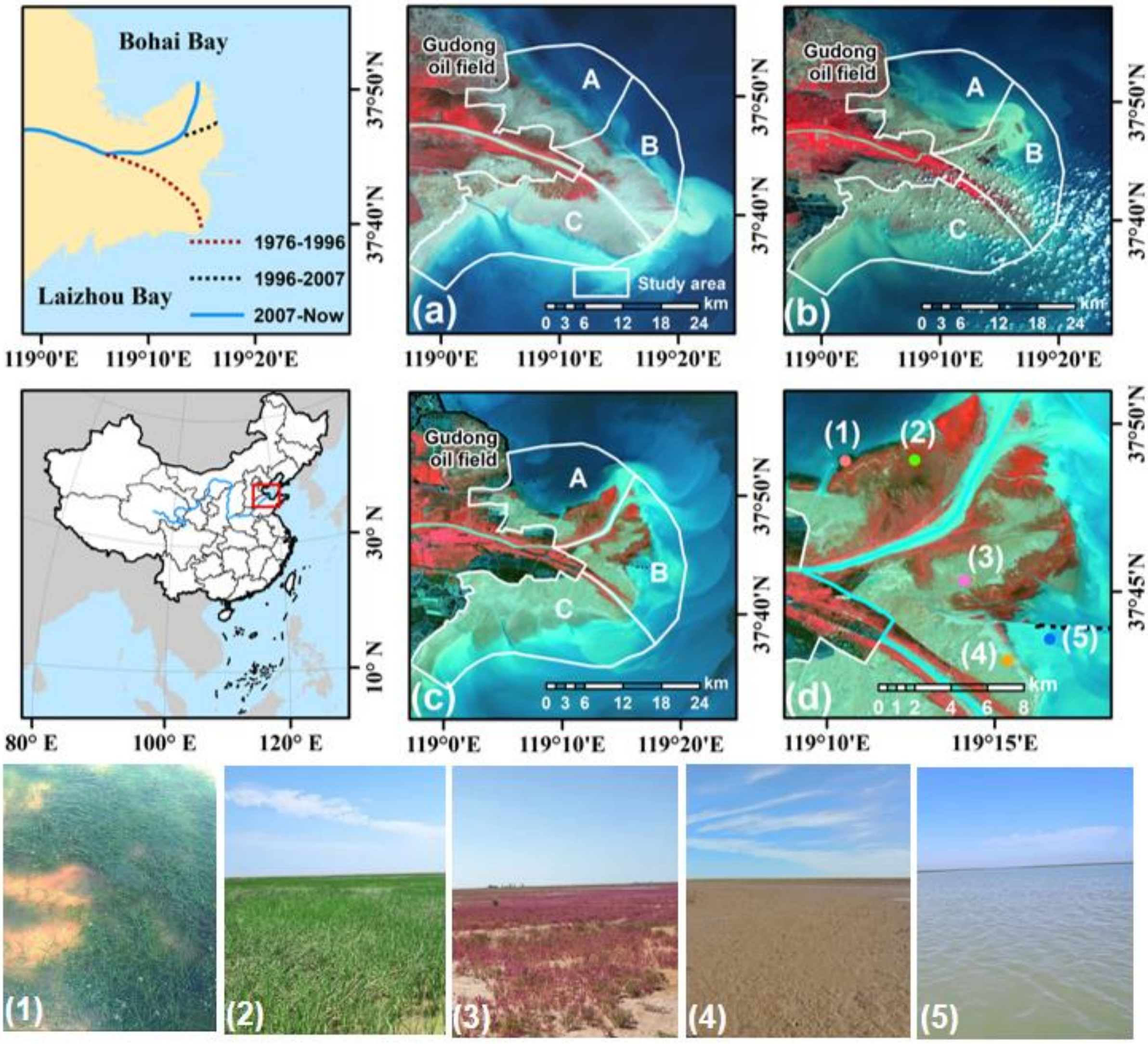

Fig. 1. The location of the study area. (a) – (c) are Landsat imagery in standard false color acquired on August 27, 1993; August 5, 2003; August 10, 2016, respectively. (d) illustrates the spatial locations of field photos. Field photos in (1) - (5) are *Z. japonica*, *S. alterniflora*, *S.salsa*, tidal flat, and water, respectively.

2.2 Datasets

2.2.1 Landsat imagery and pre-processing

We collected all available Landsat 5 TM, Landsat 7 ETM+ and Landsat 8 OLI surface reflectance (SR) images (Tire 1 Level 2 products) covering YRD (Path 121, Row 43) during

1985-2018 on the Google Earth Engine platform, with a total number of 801 images. The SR products were generated by atmospheric correction using Landsat Ecosystem Disturbance Adaptive Processing System (LEDAPS) and Landsat Surface Reflectance Code (LaSRC) algorithms. For each image, the quality assurance (QA) band was used to mask out the bad-quality pixels covered by cloud, cirrus, shadow, and snow. We grouped the time-series observations during 34 years into 16 periods to ensure each period has enough valid observations in each season (Fig. 2). In general, observations during every two-year period were grouped except for 1993-1998. Because the river tail channel shifted in 1996, we grouped observations before and after tail channel shift in to two periods, i.e., from 1993 to 1995 and from 1996 to 1998, respectively. Fig. 2 shows the available Landsat images by sensors range from 24 to 75, and the average number of valid observations ranges from 10 to 40 in the 16 periods (Fig. 2a). Most pixels have at least one observation during the summer (June to August) and autumn (September to November), and the autumn witnessed slightly more valid observations than the summer (Fig. 2 b-d).

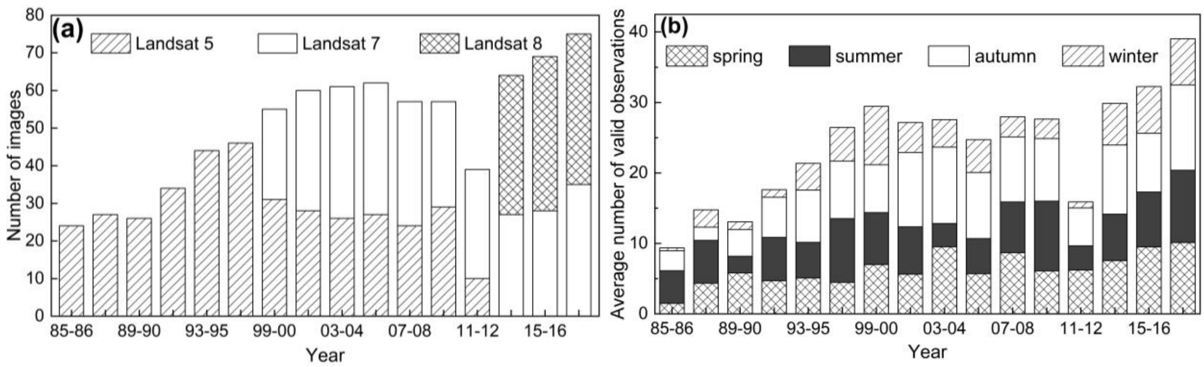

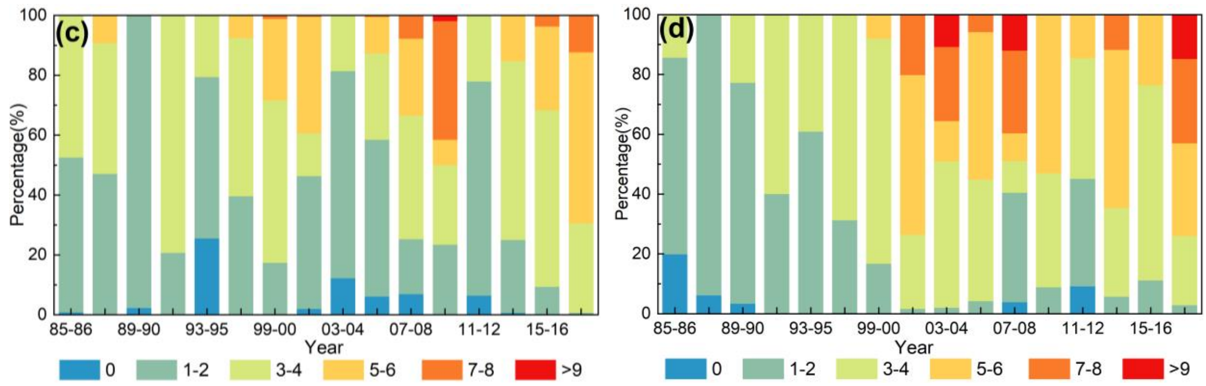

Fig. 2 The number of Landsat images (a) by sensors (Landsat TM, Landsat ETM+, Landsat OLI), (b) by seasons (spring from March to May, summer from June to August, autumn from September to November, and winter from December to February), and percentage of pixels with various numbers of good-quality observations in (c) summer and (d) autumn on YRD in each period during 1985-2018.

2.2.2 Field investigations and high spatial resolution imagery

In August 2016, July 2017, and June 2018, we conducted several field investigations in the seagrass bed habitats in the study area. During each survey, we recorded the locations of *Z. japonica* patches using GPS RTK units. High spatial resolution imagery including Gaofen-1 (GF-1, 2 m), Gaofen-2 (GF-2, 1 m) and Sentinel-2 (10 m) images were used to examine the appearance of *Z. japonica* and other salt marsh species on the image. Visual analysis of these images helped us locate *Z. japonica* on the images in other years when field surveys were not carried out. In addition, we collected WordView-2 (0.5 m), ZY-3 (6 m), SPOT-6 (1.5 m), and GF-1/2 high spatial resolution imagery during June-October from 2012 to 2018 (Table 1). Because of the scarcity of high-resolution data before 2012, we relied on Landsat satellite images for visual interpretation. These images, together with the field investigation records were used to create reference samples in order to analyze the phenological dynamics of typical vegetation species in the study area (see Section 3.2) and to validate the seagrass mapping results (Section 3.5).

Table 1. High spatial resolution imagery used for validation sample collection from 2012 to 2018.

Year	Date	Satellite sensors	Spatial resolution (m)
2018	June 5 to October 27	GF-1; GF-2	2; 1
2017	June 9 to November 4	GF-1; GF-2	2; 1
2016	June 22 to October 14	GF-1; GF-2	2; 1
2015	May 25 to October 27	GF-1; GF-2	2; 1
2014	June 6 to October 28	GF-1	2
2013	June 14 to October 17	GF-1; SPOT 6	2; 1.5
2012	May 27 to September 20	WorldView-2; ZY-3	0.5; 6

3 Methods

Fig. 3 illustrates the workflow of *Z. japonica* seagrass beds mapping. First, potential distribution area of *Z. japonica* in YRD was delineated based on time-series Landsat images during each period (section 3.1). Second, SGI that considers both spectral and phenological characteristics of *Z. japonica* was developed by analyzing time-series spectral indices (section 3.2). Third, separability analysis was conducted to evaluate the reliability of SGI (Section 3.3). Fourth, SGI images were generated within the seagrass potential area for each period and an unsupervised classification method was developed for seagrass identification (section 3.4); Finally, the seagrass mapping results were validated and seagrass maps during 1985-2018 were generated for YRD (Section 3.5).

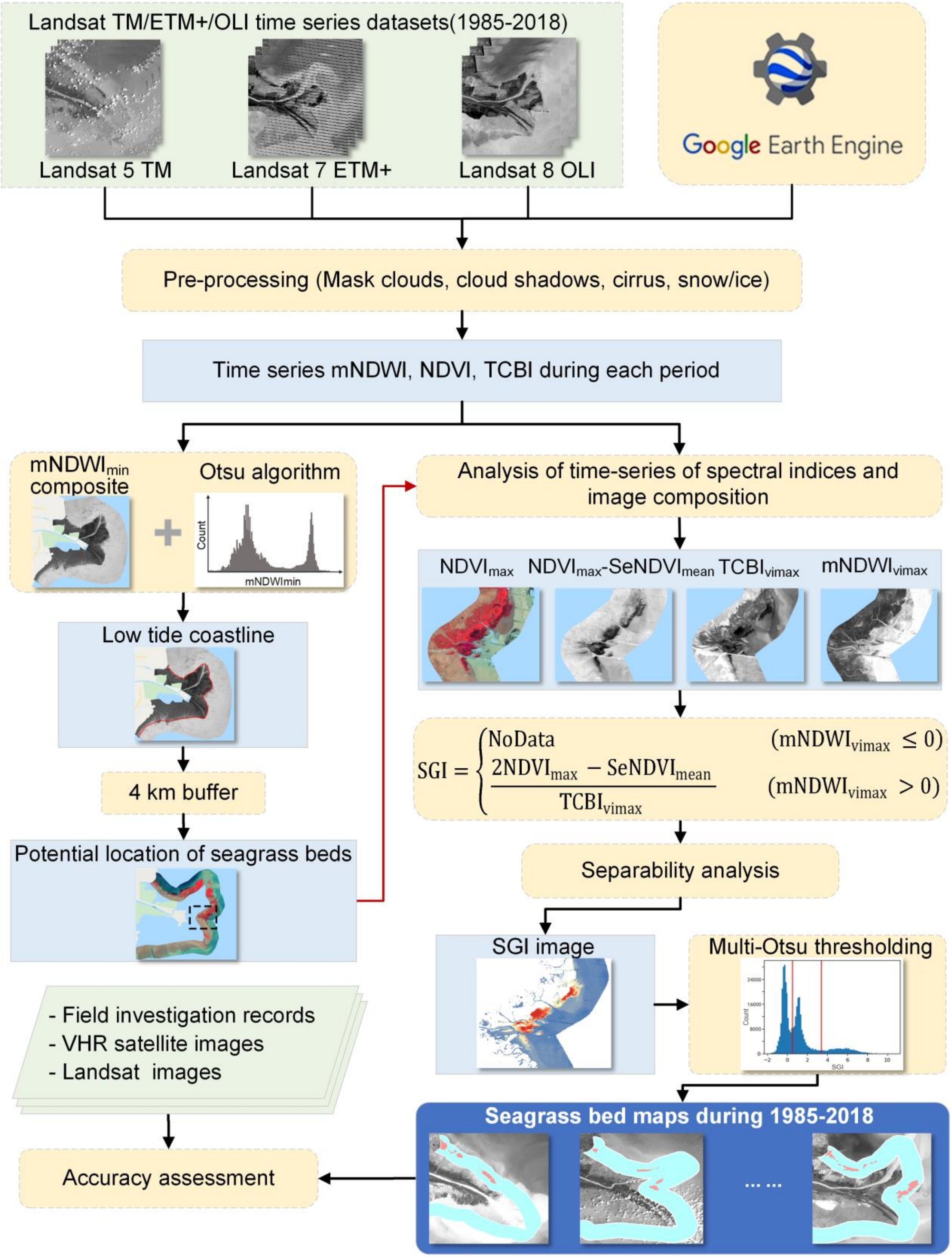

Fig.3 Workflow of seagrass beds mapping.

3.1 Identify potential distribution area of seagrass beds

According to our field surveys and previous reports (Zhou et al., 2016; Zhang et al., 2019), *Z. japonica* grows in the low intertidal zone of YRD within 500 m away from the coastline. In order to narrow down the image processing extent and reduce the influences of land cover types in the high tidal zone, we created 4 km buffer area around the coastline (2 km inside and outside the coastline) as the potential distribution area of *Z. japonica*.

We delineated coastline for each period based on the minimum composite image of Modified Normalized Difference Water Index (mNDWI) (hereafter $mNDWI_{min}$). mNDWI (Eq. 1) is sensitive to open surface water bodies, and it can identify subtle differences between turbid and clear water (Xu, 2005). At present, mNDWI is one of the most widely used indices for coastline extraction.

$$mNDWI = \frac{\rho_{green} - \rho_{SWIR1}}{\rho_{green} + \rho_{SWIR1}} \tag{1}$$

where ρ_{green} is the reflectance of the green band (Band 2 for Landsat TM/ETM+ and Band 3 for Landsat OLI), and ρ_{SWIR1} is the reflectance of the short-wave infrared 1 (Band 5 for Landsat TM/ETM+ and Band 6 for Landsat OLI). First, mNDWI was calculated from each Landsat image. Based on all mNDWI images during each period, we generated an $mNDWI_{min}$ image, where the value at each pixel represents the lowest mNDWI during the period. The $mNDWI_{min}$ image depicts the driest condition of every pixel. Then, Otsu algorithm was used to separate land from water on $mNDWI_{min}$ image and extract the coastline. The Otsu algorithm is a nonparametric approach for image thresholding. The optimal threshold is determined by traversing all potential thresholds using the image's histogram and selecting the one with the minimal inter-class variation (Otsu, 1979). As $mNDWI_{min}$ generally represents the image at the lowest tide, the delineated coastline and the 4 km buffer area can effectively remove the features at mid to high tide area. As a results, the potential distribution area of *Z. japonica* was identified for every periods. By field surveys and visual interpretation of the reference images, land cover categories in the area consists of include *Z. japonica*, *S. alterniflora* (only after 2008), *S.salsa*, tidal flat and water.

3.2 Construct seagrass index (SGI)

3.2.1 Analysis of time-series spectral indices

To enhance the separability between *Z. japonica* seagrass and other cover types (*S. alterniflora*, *S.salsa*, tidal flat and water), time series analysis of three spectral indices including NDVI, mNDWI and Tasseled Cap Brightness Index (TCBI) was conducted. NDVI has been widely used to represent growing status of vegetation, with NDVI reaching peak during growing season and declining during senescence season. mNDWI was selected as it is sensitive to water features mixed with vegetation (Singh et al., 2015). TCBI was derived from Tasseled Cap Transformation, which incorporates six different bands of Landsat TM/ETM+/OLI imagery (Kauth, 1976). The TCBI has proven to be suitable for soil moisture estimation and inundation detection (Ludwig et al., 2019).

Fig. 4 illustrates time-series NDVI, mNDWI and TCBI of pure *Z. japonica*, *S. alterniflora*, *S.salsa*, tidal flat and water pixels calculated based on valid observations during 2015-2016. We merged all observations during 2015-2016 sorted by the day of year (DOY). Fig. 4a shows that the NDVI of *Z. japonica* depicts water-like characteristics during late September-May

(NDVI<0) and strong vegetation features during June-August. It climbs from June to August, with NDVI peak occurring in August, and then rapidly declines to negative values in the end of September. We determined the DOY from 150 to 250 as the green period (Gr-P) and DOY from 260 to 330 as the senescence period (Se-P) of *Z. japonica*. The penology pattern of *Z. japonica* observed from the NDVI time series is consistent with previous in-situ studies (Zhang et al., 2019; Zhang et al., 2021). During Gr-P, *Z. japonica* demonstrates similar NDVI as *S. alterniflora*. During Se-P, *Z. japonica* demonstrates significantly lower NDVI than *S. alterniflora* and *S. salsa*. Note that *S.salsa* shows low NDVI throughout the year because of its short plant height and low coverage, with peak value of around 0.3 in September. The mNDWI and TCBI time series do not show much temporal variations throughout the year (Fig. 4b and 4c). *Z. japonica* has high mNDWI values. *S. alterniflora* and *S. salsa* has much lower mNDWI (mostly negative) than other types, and *Z. japonica* pixel generally has the lowest TCBI values. *S. salsa* had the highest TCBI. Due to the turbidity of the water in the YRD, the TCBI of the water is higher than that of *Z. japonica*.

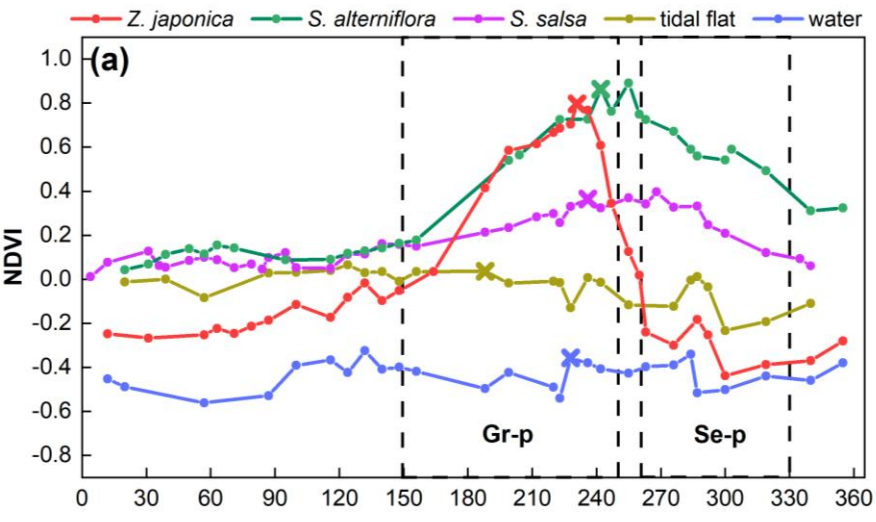

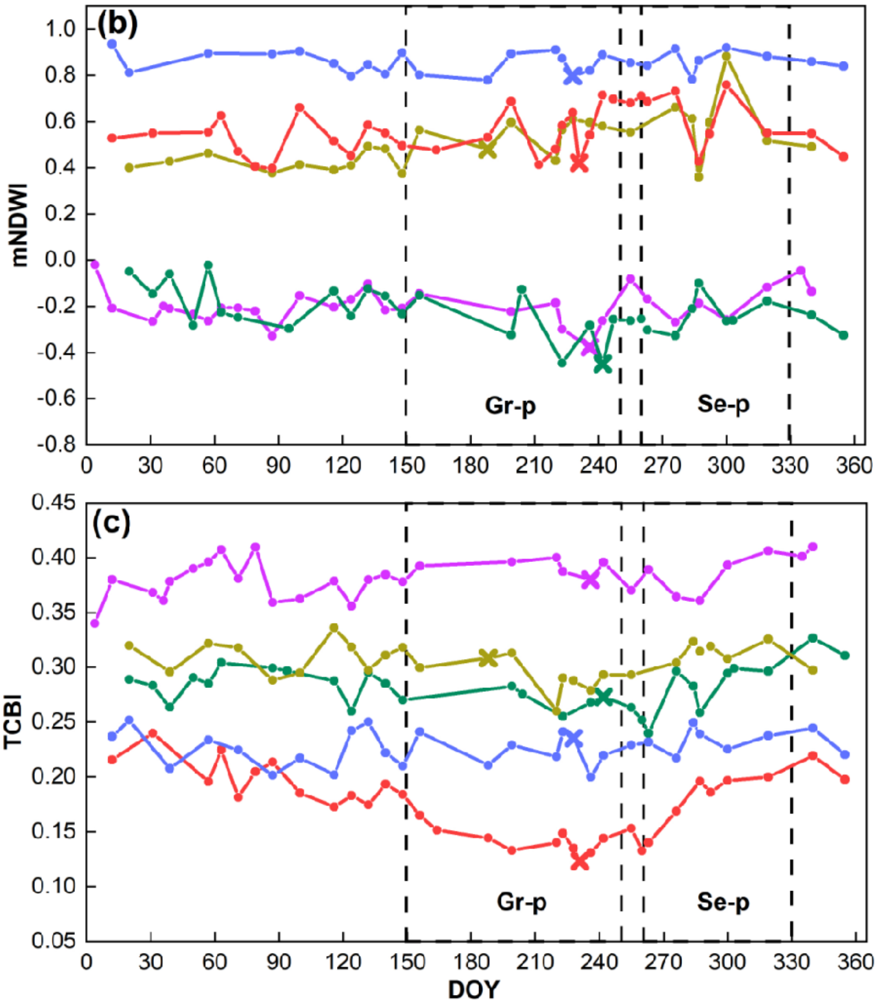

Fig. 4. The temporal profile of (a) NDVI (b) mNDWI (c) TCBI of *Z. japonica*, *S. alterniflora*, *S. salsa*, tidal flat and water pixel during 2015-2016. The maximum NDVI value was marked as ×; and the corresponding mNDWI and TCBI values on the date when NDVI reaches the maximum were also marked as ×.

Fig. 4 shows that the combination of NDVI, mNDWI and TCBI can help discriminate *Z. japonica* from others at the pixel level. The maximum NDVI ($NDVI_{max}$) during each 2 or 3-year period (marked as × in Fig. 4a) represents the greenest state of seagrass beds and thus reduces the tidal influence and possible cloud contamination in a single image. However, using the $NDVI_{max}$ alone cannot discriminate *Z. japonica* from *S. alterniflora* as they have similar $NDVI_{max}$ values (Fig. 4a). Note that *Z. japonica* has shorter green period than the intertidal salt marshes, and NDVI shows more rapid and higher magnitude of declination during senescence period. Therefore, we consider to use $NDVI_{max}$ to differentiate *Z. japonica* from non-vegetation types and use the difference between $NDVI_{max}$ and the mean NDVI during senescence period ($SeNDVI_{mean}$) to differentiate *Z. japonica* and other salt marshes. When NDVI of *S. alterniflora* reaches the maximum, its mNDWI reaches the lowest (mNDWI = -0.4). This is because *S. alterniflora* has dense and tall plants, therefore, depicts terrestrial vegetation spectral characteristics during growing peak.

For each 2 or 3-year period, we generated the $NDVI_{max}$ composite image using function "imageCollection.qualityMosaic" on GEE platform. Each band of the $NDVI_{max}$ image represents the band values for each pixel when NDVI reaches the maximum. Based on this image, mNDWI ($mNDWI_{vimax}$) and TCBI ($TCBI_{vimax}$) images were derived (illustrated as × in Fig. 4b and 4c at pixel level). We also generated $SeNDVI_{mean}$ image composite and derived $NDVI_{max} - SeNDVI_{mean}$ layer. In order to examine the variation in $NDVI_{max}$, $mNDWI_{vimax}$, $TCBI_{vimax}$, and $NDVI_{max} - SeNDVI_{mean}$ indices of the land cover types, we generated 1000 reference sample points for each land cover type over the 16 periods (around 63 samples for each period for each class) using field survey data and visual interpretation of reference images. As shown in Fig. 5, $NDVI_{max}$ of *Z. japonica* seagrass beds demonstrates large variations, ranging from 0.21 to 0.89. The histogram of $NDVI_{max}$ of *Z. japonica* overlaps with that of *S. alterniflora* in the right tail and that of *S. salsa* in the left tail (Fig. 5a). $mNDWI_{vimax}$ can effectively distinguish *Z. japonica* from *S. alterniflora* because almost all *Z. japonica* sample pixels have positive $mNDWI_{vimax}$ and *S. alterniflora* sample pixels have negative $mNDWI_{vimax}$. However, $mNDWI_{vimax}$ cannot separate *Z. japonica* from *S. salsa* (Fig 5b). Note that *S. salsa* grows on both mid-high intertidal area and low intertidal area, for *S. salsa* on tidal flats near the water, $mNDWI_{vimax}$ is greater than 0 due to tidal influence. Fig. 5c shows that the $TCBI_{vimax}$ of *Z. japonica* is considerably lower than that of *S. salsa*, while its histogram has obvious overlap with water and tidal flat. The $NDVI_{max} - SeNDVI_{mean}$ of *Z. japonica* is greater than other land cover types (Fig. 5d), while its histogram has small overlap with *S. alterniflora*.

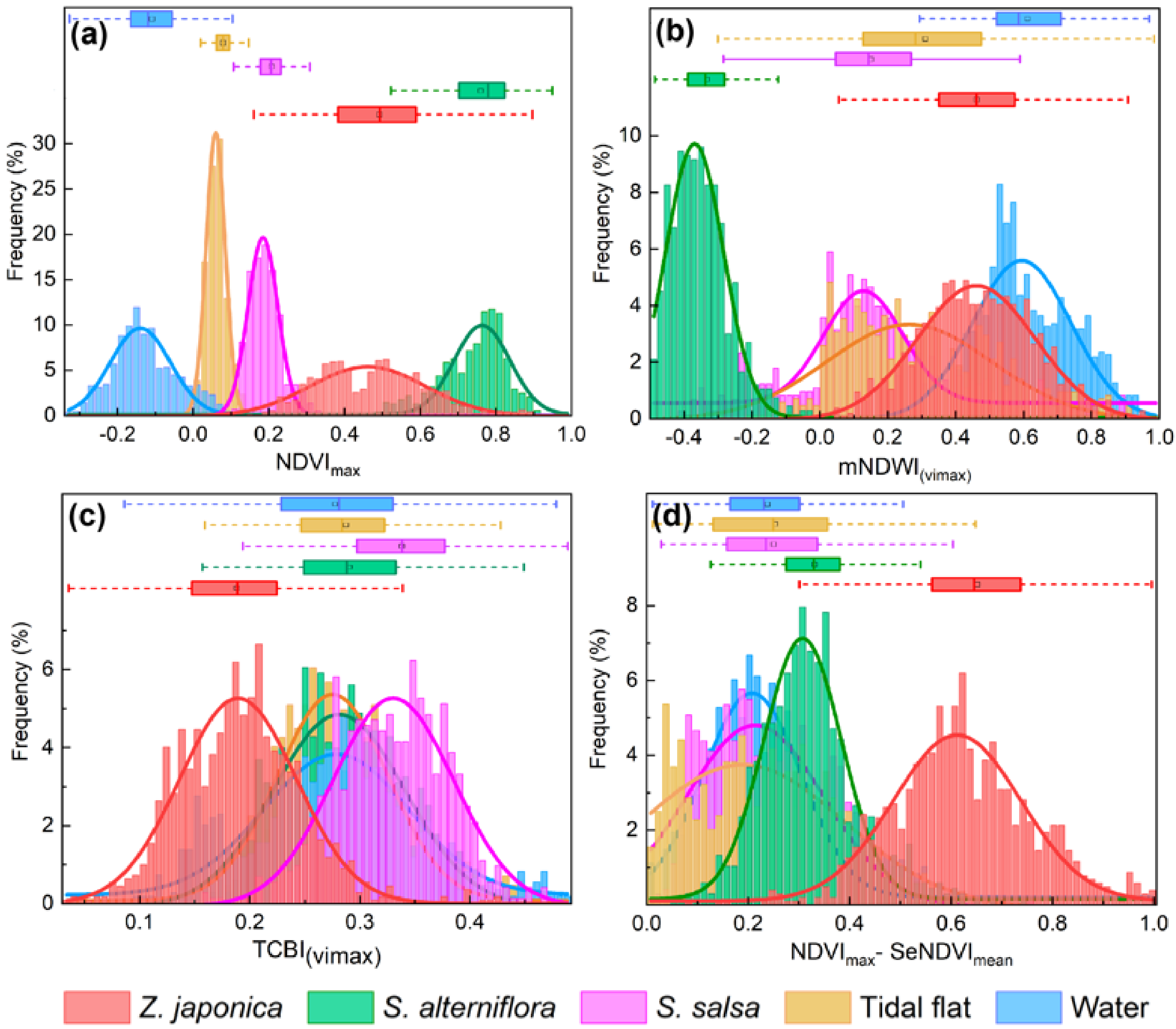

Fig. 5 Histograms and box plots of (a) $NDVI_{max}$, (b) $mNDWI_{vimax}$, (c) $TCBI_{vimax}$, (d) $NDVI_{max}$-$SeNDVI_{mean}$ for *Z. japonica*, *S. alterniflora*, *S. salsa*, tidal flat and water.

3.2.2 Formulation of SGI based on phenological-spectral characteristics

Based on the above analysis, we can utilize $mNDWI_{vimax} > 0$ to remove *S. alterniflora* from the image. Compared to tidal flat and water, *Z. japonica* has much higher $NDVI_{max}$. Compared to *S. salsa*, it has higher $NDVI_{max} - SeNDVI_{mean}$ and lower $TCBI_{vimax}$. To enhance the contrast, we formulated SGI as Eq. (4). We first assigned $NoData$ value to the pixels with $mNDWI_{vimax} \leq 0$ as all *Z. japonica* pixels have positive $mNDWI_{vimax}$ values.

For other pixels, we sum $NDVI_{max}$ and $NDVI_{max} - SeNDVI_{mean}$ in the numerator to highlight the spectral and phenological characteristics of *Z. japonica* and use $TCBI_{vimax}$ in the denominator to differentiate with *S. salsa*.

$$SGI = \begin{cases} NoData & (mNDWI_{vimax} \leq 0) \\ \dfrac{2NDVI_{max} - SeNDVI_{mean}}{TCBI_{vimax}} & (mNDWI_{vimax} > 0) \end{cases} \quad (4)$$

Fig. 6 shows that the histogram of SGI of *Z. japonica*, water, *S. salsa* and tidal flats sample pixels show three peaks. *Z. japonica* has obviously higher SGI than *S. salsa*, tidal flat and water. Water pixels have relatively lower SGI than other types, while *S. salsa* and tidal flats have similar SGIs. Overall, the SGI histogram of *Z. japonica* is visually more separable from others compared to any of $NDVI_{max}$, $NDVI_{max} - SeNDVI_{mean}$ or $TCBI_{vimax}$ (Fig. 5).

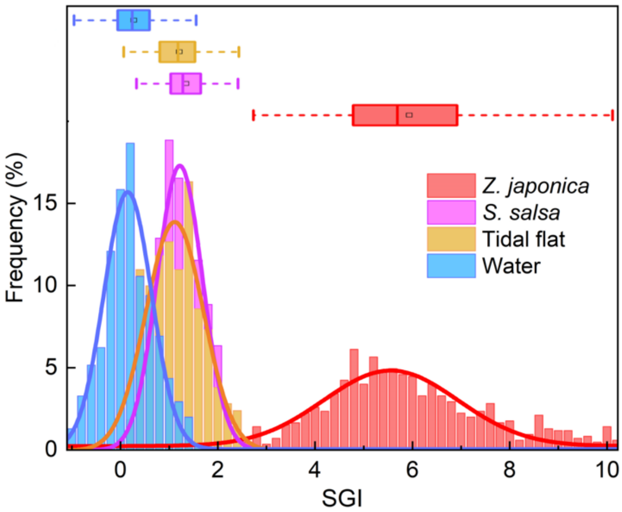

Fig. 6 Histogram and box plot of SGI index for *Z. japonica*, *S. salsa*, tidal flat and water.

3.3 Separability analysis

Separability analysis is important to examine how well a target class can be discriminated from others and can be used as indicators of the classification performances (Xu et al., 2021). In this study, we utilized separability index (SI) presented by Somers and Asner (Somers et al.,

2010) to assess and compare the separability between *Z. japonica* and others in terms of $NDVI_{max}$, $mNDWI_{vimax}$, $NDVI_{max} - SeNDVI_{mean}$, $TCBI_{vimax}$ and SGI. SI incorporates both intra-class and inter-class variabilities. The formula is as follows:

$$SI_{zo} = \frac{\Delta inter_{zo}}{\Delta intra_{zo}} = \frac{|\overline{\mu_z} - \overline{\mu_o}|}{1.96 \times (\sigma_z + \sigma_o)} \quad (5)$$

where SI_{zo} denotes the separability index between *Z. japonica* and other categories. $\overline{\mu_z}$ and $\overline{\mu_o}$ denote the mean index values of *Z. japonica* and the other class, respectively. σ_z and σ_o denote the standard deviation of the index values. $|\overline{\mu_z} - \overline{\mu_o}|$ denotes the inter-class variance between *Z. japonica* and the other class, and $(\sigma_z + \sigma_o)$ denotes the intraclass variance. Higher SI values indicates greater disparities between *Z. japonica* and others and smaller within-class variances.

3.4 Identify seagrass bed extent

We adopted multi-Otsu thresholding algorithm (Liao et al., 2001), an unsupervised clustering approach, to extract *Z. japonica* automatically based on SGI image without training process. The conventional Otsu algorithm automatically select one optimal threshold and partitions the dataset into two classes based on the histogram of the dataset. It has been successfully used for image binarization and target detection in remote sensing. Unlikely, multi-Otsu thresholding algorithm calculates multiple thresholds with the number of categories defined by user (>2). From Fig. 6, we suppose that two thresholds can be used to separate *Z. japonica*, water and tidal flat/*S. salsa* based on SGI image. In this case, multi-Otsu algorithm aims to find two thresholds which maximize the inter-class variance of SGI.

$$\sigma_t^2(t_1, t_2) = \sum_{i=1}^{3} P_i\,(\mu_i - \mu_T)^2 \quad (6)$$

$$(T_1, T_2) = arg \max_{0<T_1<T_2} \{\sigma^2(t_1, t_2)\} \quad (7)$$

$$P_i = \frac{\sum pixels\ in\ class\ i}{Total\ pixels} \quad (8)$$

where $\sigma_t^2(t_1, t_2)$ denotes the inter-class variance at threshold (t_1, t_2). The algorithm goes through all possible thresholds to find the optimal thresholds (T_1, T_2) which maximize $\sigma_t^2(t_1, t_2)$. P_i represents the probability of a pixel belonging to class *i*, μ_i represents the mean SGI value of class *i*, and μ_T represents the mean value of the whole SGI histogram. We used the multi-Otsu algorithm to segment SGI images into three classes. According to Fig. 5, the class with SGI values greater than T_2 is identified as *Z. japonica* seagrass bed. Finally, a total of 16 seagrass maps were generated by re-classifying the results in each period into two categories: *Z. japonica* and non- *Z. japonica*.

3.5 Accuracy assessment

Considering the availability of high spatial resolution imagery, we validated all *Z. japonica* seagrass maps during 2011-2018, and selected two *Z. japonica* seagrass maps before 2000 (1993-1995) and after 2000 (2007-2008) for validation. First, we employed stratified random sampling strategy to select validation samples. From the seagrass maps during each period, 150 and 300 pixels were randomly selected for *Z. japonica* and non- *Z. japonica*, respectively. The sample pixels were visually interpreted based on the field investigations during 2016-2018 combined with high spatial resolution imagery acquired between 2012 to 2018 (Table 1). Before 2010, the sample pixels were interpretated based on the time-series Landsat images. These validation pixels should have consistent class (*Z. japonica* or non- *Z. japonica*) during the two or three-year period. In rare cases that the class of a sample pixel has changed from *Z. japonica* to non- *Z. japonica* or vice versa, the sample pixel was excluded and a pixel with unchanged class around it was added.

4 Results

4.1 Separability analysis and SGI maps

Fig. 7 shows the SI values of each index including $mNDWI_{vimax}$, $NDVI_{max}$, $TCBI_{vimax}$, $NDVI_{max} - SeNDVI_{mean}$ and SGI for seagrasses between different classes based on the 1000 reference samples. It is obvious that $mNDWI_{vimax}$ has much greater SI value (1.68) between *Z. japonica* and *S. alterniflora* than other indices, indicating that *S. alterniflora* can be well separated from *Z. japonica* by $mNDWI_{vimax}$. SGI shows much greater SI values than other indices in separating *Z. japonica* from *S. salsa*, tidal flat and water (SI value = 1.42, 1.41 and 2.17 respectively). We also calculated the SI value of the 5 indices between *Z. japonica* and non-*Z. japonica*. Similarly, the SI value of SGI between *Z. japonica* and non-*Z. japonica* (SI=1.41) was higher than any other indices (0.81 for $NDVI_{max}$; 0.42 for $TCBI_{vimax}$ and 0.68 for $NDVI_{max} - SeNDVI_{mean}$;). The highest SI value of SGI between *Z. japonica* and non- *Z. japonica* indicates that SGI generates good inter-class separability and low intra-class variability.

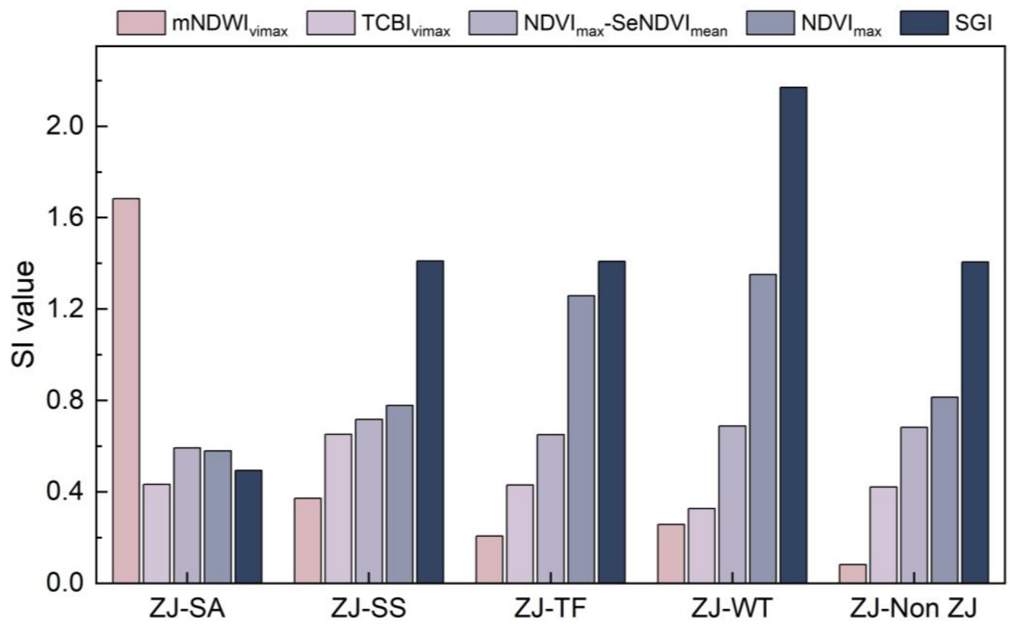

Fig.7. SI values for each index between different classes. Class acronyms are: ZJ- *Z. japonica*, SA- *S. alterniflora*, SS- *S. salsa*, TF- Tidal flat, WT- water, Non ZJ- non ZJ

Fig. 8 presents some exemplar SGI maps within the potential distribution area (left column), as well as corresponding histograms (center column) and the extracted *Z. japonica* map (right column). The SGI maps show substantially higher SGI values at the lower intertidal area around the north and east coastline of YRD. Two peaks in the low range of SGI (<3) and one flatter peak in the high range of the SGI (3~10) are observed in the histograms, which is quite similar as Fig. 6. The three-class Otsu algorithm identified two thresholds, 0.73 and 3.21 for 2013-2014 (Fig. 8a); -0.09 and 4.07 for 2003-2004 (Fig. 8b); 0.46 and 3.16 for 1993-1995 (Fig. 8c), and the pixels with SGI greater than 3.21, 4.07, 3.16 were classified as *Z. japonica* seagrass beds, respectively. Fig. 9 illustrates that the SGI thresholds for *Z. japonica* identification are relatively stable, varying from 2.22 to 4.11 with an average threshold of 3.22. The SGI thresholds for the images before 2001 (2.22~3.16) were slightly lower than those after

2001 (3.18~4.11). Examinations of the images showed that the seagrass beds demonstrated lower $NDVI_{max}$ in those years than other years, which might be explained by lower biomass or coverage.

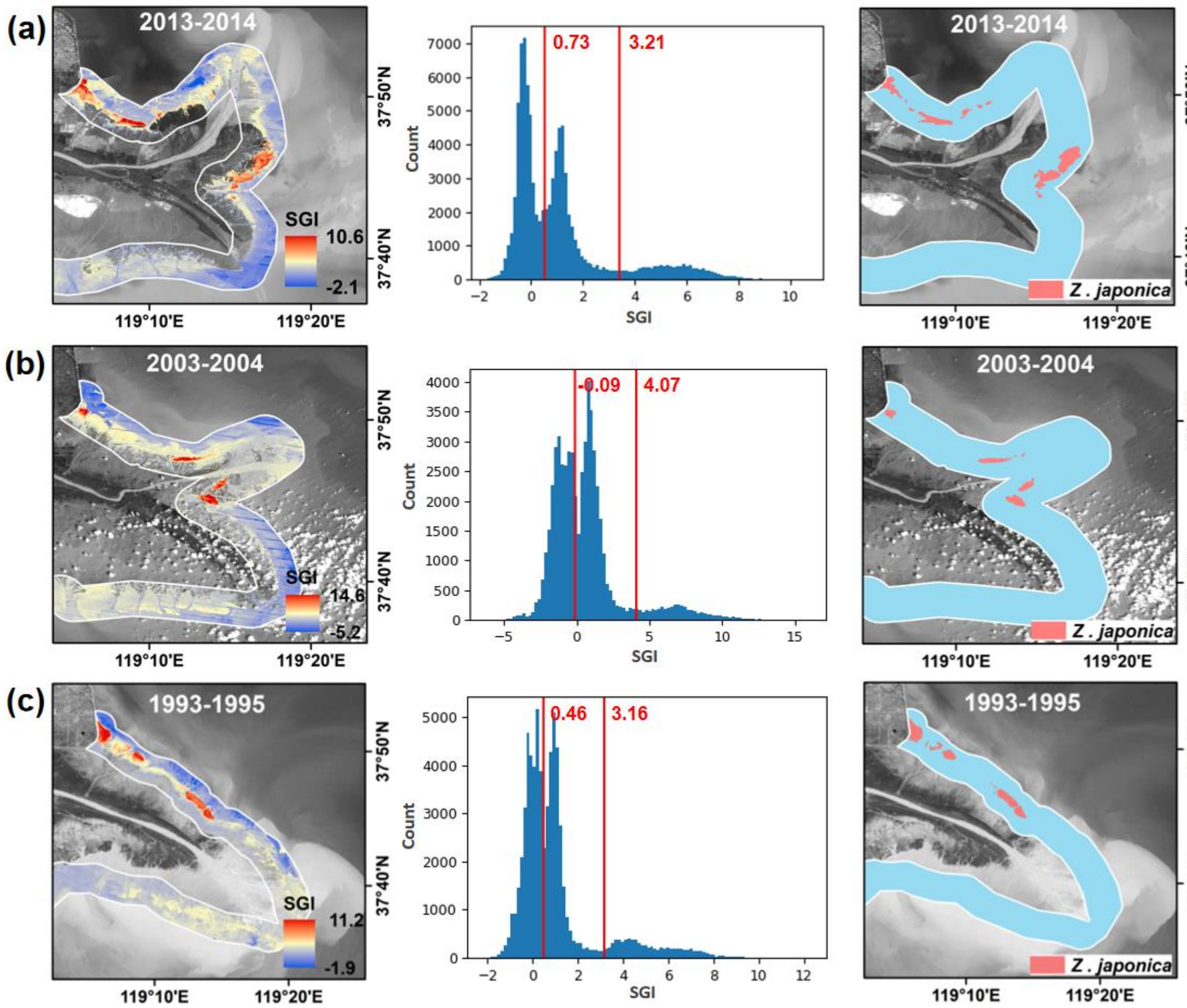

Fig. 8. SGI maps in the potential distribution area (left column), the corresponding SGI histogram and the thresholds identified by multi-Otsu algorithm (center column), and the classification results of *Z. japonica* (right column) in (a) 2013-2014, (b)2003-2004, (c)1993-1995.

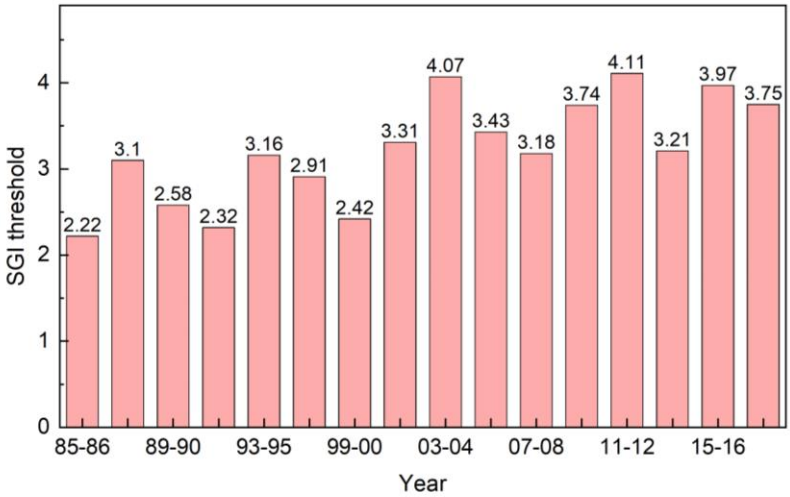

Fig. 9. SGI thresholds for *Z. japonica* extraction in each period during 1985-2018. The area with SGI greater than the threshold is identified as *Z. japonica*.

4.2 Accuracy assessment of seagrass bed maps

Table 2 lists the *Z. japonica* seagrass mapping accuracies in 1993-1995, 2007-2008, 2011-2012, 2013-2014, 2015-2016, and 2017-2018. The overall accuracies of the seagrass bed maps are higher than 95%, and the kappa coefficients are above 89%. The user's accuracies of *Z. japonica* seagrass bed are generally higher than 94.67%, indicating very small commission errors. The producer's accuracies of seagrass beds are higher than 95.33% except for 2015-2016. In 2015-2016, the producer's accuracy is 90.06%, suggesting omission errors of around 10%. Examinations of Landsat images in 2015-2016 found that frequent cloud cover in both years may have resulted in insufficient acquisition of effective image pixels at low tide during the green period. Overall, the validation results show that the seagrass maps generated from SGI and multi-Otsu thresholding algorithm are accurate for further analysis of spatiotemporal dynamics of *Z. japonica* distribution.

Table 2. Confusion matrix of *Z. japonica* seagrass bed (ZJ) maps accuracy assessment. PA=

producer's accuracy; UA = user's accuracy; OA = overall accuracy.

Year	Class	Ground truth samples (pixels)		PA (%)	UA (%)	OA (%)	Kappa
		ZJ	Non-ZJ				
1993-1995	ZJ	148	2	95.48	98.67	98.00	95.54
	Non-ZJ	7	293	99.32	97.67		
2007-2008	ZJ	142	8	98.61	94.67	97.78	94.95
	Non-ZJ	2	298	97.39	99.33		
2011-2012	ZJ	143	7	95.33	95.33	96.89	93.0
	Non-ZJ	7	293	97.67	97.67		
2013-2014	ZJ	147	3	95.45	98.0	97.76	95.03
	Non-ZJ	7	293	98.99	97.67		
2015-2016	ZJ	145	5	90.06	96.67	95.33	89.69
	Non-ZJ	16	284	98.27	94.67		
2017-2018	ZJ	144	6	99.31	96.0	98.44	96.47
	Non-ZJ	1	299	98.03	99.67		

4.3 Spatial-temporal dynamics of *Z. japonica* seagrass bed

Fig. 10 shows that the area of *Z. japonica* fluctuated greatly, ranging from 149 ha in 2005-2006 to 1302.9 ha in 2011-2012. From 1985 to 1995, the area of *Z. japonica* generally showed an increasing trend from 762.2 ha in 1985-1986 to 1060.9 has in 1993-1995, except that only 374.9 ha was detected in 1989-1990. From 1996 to 2010, the area of *Z. japonica* varied from 149.0 ha to 924.6 ha. From 2011 to 2018, the area presented obvious decreasing trend, from 1302.9 ha to 332.3 ha in 2017-2018. During the 34 years, no *Z. japonica* was detected in Zone C. *Z. japonica* was distributed in zone A throughout the 34 years but showed an overall decreasing trend. Before 1999, Zone A had an average area of 904.4 ha *Z. japonica* except for 1989-1990, when only 374.3 ha of *Z. japonica* was detected. After 1999, the average *Z. japonica* area was 652.2 ha. *Z. japonica* first appeared in Zone B in 1991. The area varied from 10 ha in 2005-2006 to 822 ha in 2011-2012. From 2011 to 2018, the area of *Z. japonica* decreased to

166.1 ha. In 2001-2004 and 2009-2018, the area in Zone B exceeded that in Zone A.

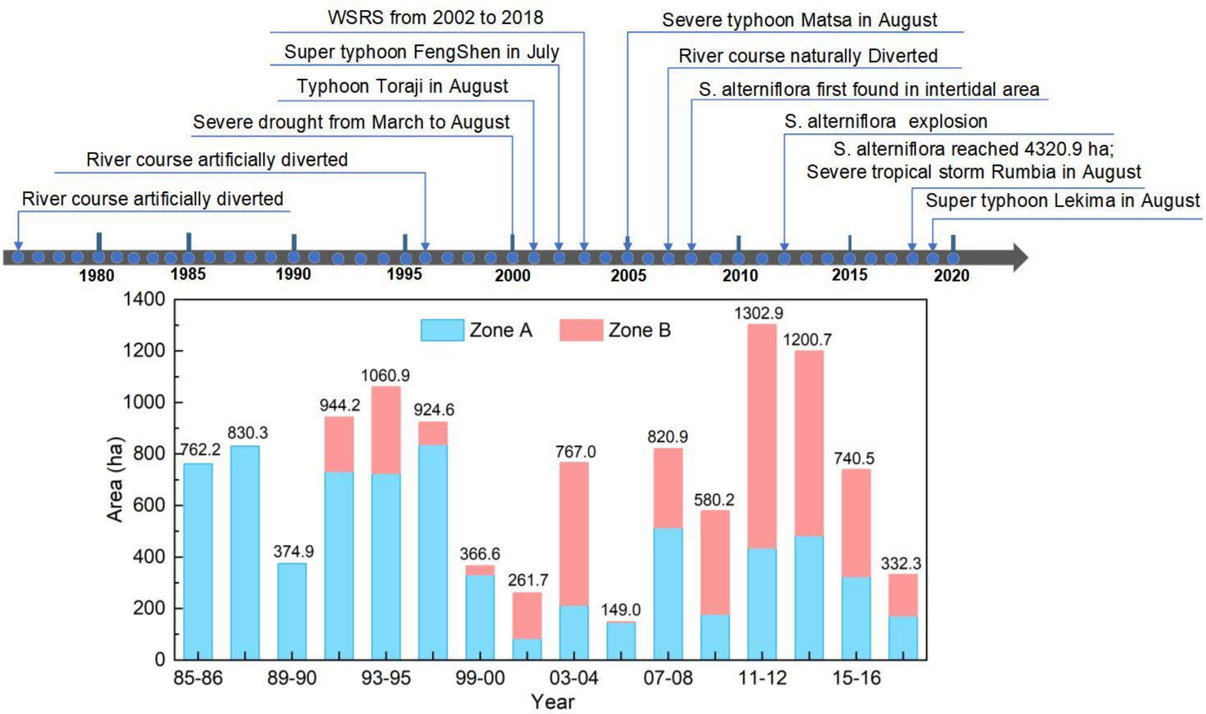

Fig. 10. *Z. japonica* area during 1985-2018 and timeline of important events in YRD.

4.3.1 Spatial distribution of seagrass bed before and after river course diversion

The river course of the Yellow River shifted twice in YRD during 1985-2018. The first shift occured in 1996 when the Q8 channel was artifically constructed and the river course migrated from the southeastward to the eastward. The second one occurred in 2007, with the end of the channel natually shifted northward. Fig.11 presents the *Z. japonica* seagrass maps during 1985-2018, superimposed on the flase color Landsat imagery acquired in growing season. The Landsat imagery illustrates that the morphology of the shorelines changed significantly after each river channel shift, and the spatial distribution of *Z. japonica* changed accordingly. In 1985, only one large patch of *Z. japonica* was detected in the east of the artificial coastline of Gudong Oil Field. Since 1985, this patch shrank substantially (Fig. 11). From 1985 to 1996, the shoreline around the river mouth extended southeastward for aournd 4.5 km. Correspondingly, new patches of *Z. japonica* grew in the northern intertidal area from 1991 to 1995 (marked as ① in Zone B in Fig. 11 d-e).

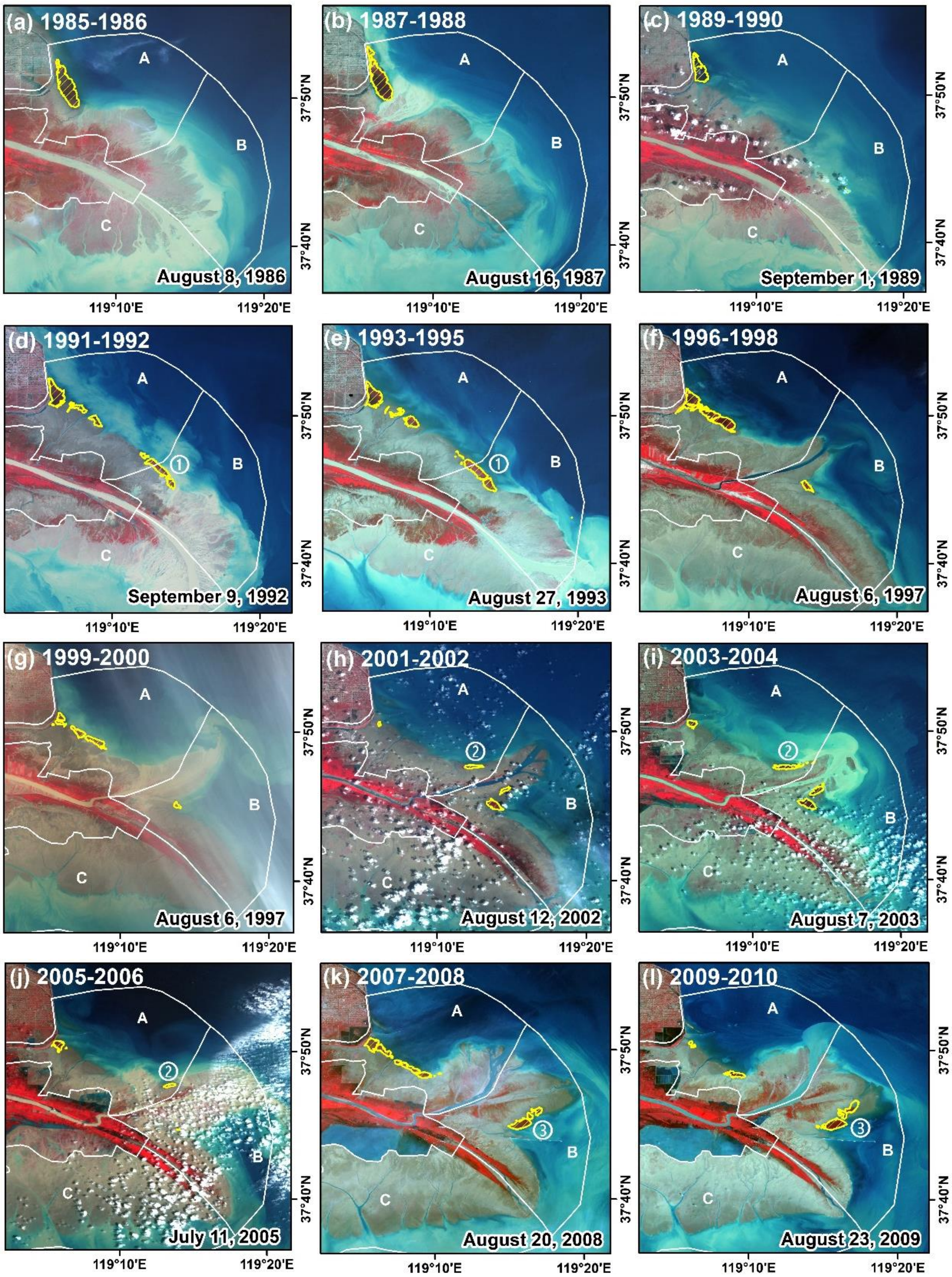

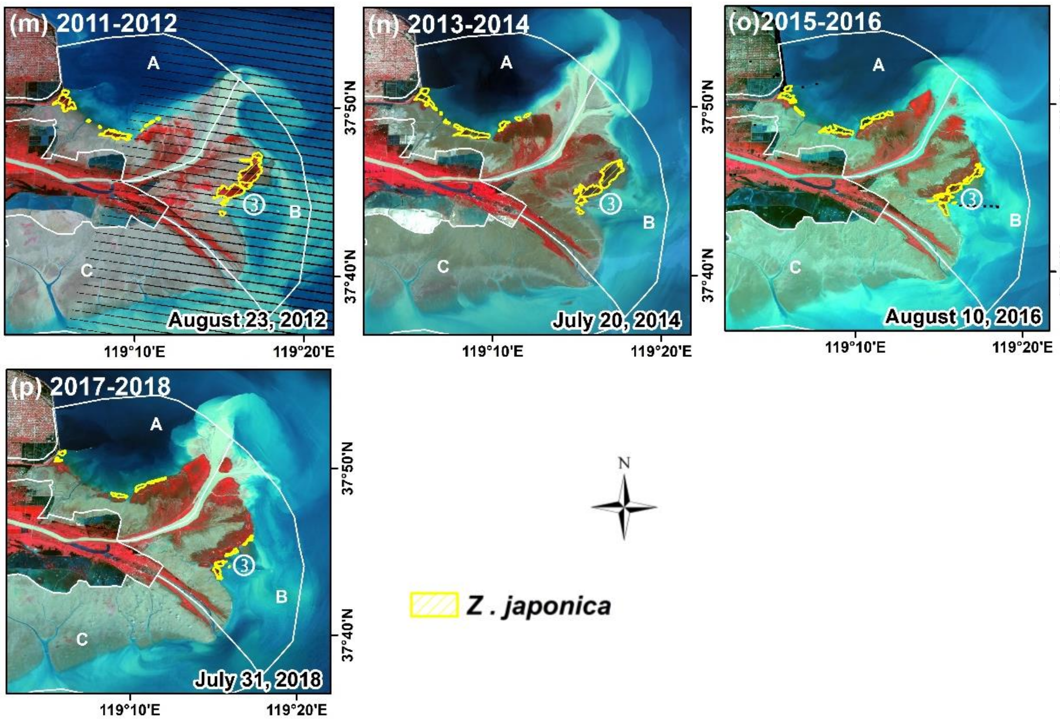

Fig. 11. Spatial distribution of *Z. japonica* seagrass bed in YRD.

In 1996, a large part of the patch in Zone B disappeared when the tidal flat formed with the sediment deposition during the river course diversion. Only a small patch remained in 1996 and then expanded from 1999 to 2004. After 1996, the river mouth extended eastwards. Correspondingly, a big patch of *Z. japonica* was observed in the newly formed intertidal area of the north shoreline from 2001 (marked as ② in Fig. 11h). In 2002, Yellow River Conservancy Commission (YRCC) initiated water sediment regulation scheme (WSRS), aiming to sour the elevated riverbed in the lower Yellow River and maintaining the storage capacity in the reservoirs in the downstream of Yellow River. From 2002 to 2018 except for 2016 and 2017, WSRS was implemented every summer by creating man-made flood peak and expelling accumulated sediment from the large reservoirs (e.g., Xiaolangdi Reservoir). During WSRS, significant increase in water and sediment delivery was observed and thus the sediment deposition in the estuary resulted in rapid land gain in YRD (Li et al., 2019). Fig. 11 i-j illustrates substantial expansion of tidal flats in YRD during the early stage of WSRS (2003-2006). This might cause *Z. japonica* seeds to be buried by the rapid deposition of sediments, resulting in shrinkage of *Z. japonica* segrass beds patches in 2005-2006 (Fig. 11j). In 2007, the flow channel in the river mouth diverted naturally to the northward, which again changed the mophology of the shoreline in the river mouth (Fig. 11k). The rapid deposition of sediments caused the damage of *Z. japonica* bed in the north bank of the new river mouth (Fig. 11k), while new patches started to grow in 2011 (Fig. 11m). From 2007 to 2018, the northeastern shoreline continued extending to the sea, while the eastern shoreline retreated toward the land. The *Z. japonica* seagrass beds in the southeastern bank remained relatively stable (marked as ③ in Fig. 10k-p).

4.3.2 Changes of seagrass beds after *S. alterniflora* invasion

S. alterniflora was first discovered in the YRD's intertidal zone in 2008. Since then, the invasion of *S. alterniflora* has experienced three stages: slow expansion during incubation period before 2011, rapid expansion during outbreak period from 2011 to 2017, and slower expansion after 2017 (Ren et al., 2019; Wang et al., 2021). By 2019, the area of *S. alterniflora* reached 4672.38 ha (Wang et al., 2021). *S. alterniflora* expanded both landward and seaward. As illustrated in Fig. 12, before 2011, only small patches of *S. alterniflora* were found in the north bank of YRD. After 2011, *S. alterniflora* expanded rapidly to the seaward in both north bank and south bank of YRD, and started to enchroach the habitat of *Z. japonica* since 2013. Correspondingly, the seagrass bed patches shrank substantially from 2013 to 2018, especially in the south bank of YRD. Fig. 10 showed that the area of *Z. japonica* decreased from 1302.9

ha in 2011 to 332.3 ha in 2018. This is consistent with previous report by Wang et al. (2021) that *S. alterniflora* has enchroached *Z. japonica* seagrass by around 902.32 ha. On the Landsat image acquired during growing season in 2019 and 2020, no obvious patches of *Z. japonica* seagrass beds were deteced (Fig. 12f). Our field investigations also showed that no large patches of *Z. japonica* were found in 2019 and 2020. In summer 2021, the investigators could hardly find intact *Z. japonica* patches which is larger than 1 m^2.

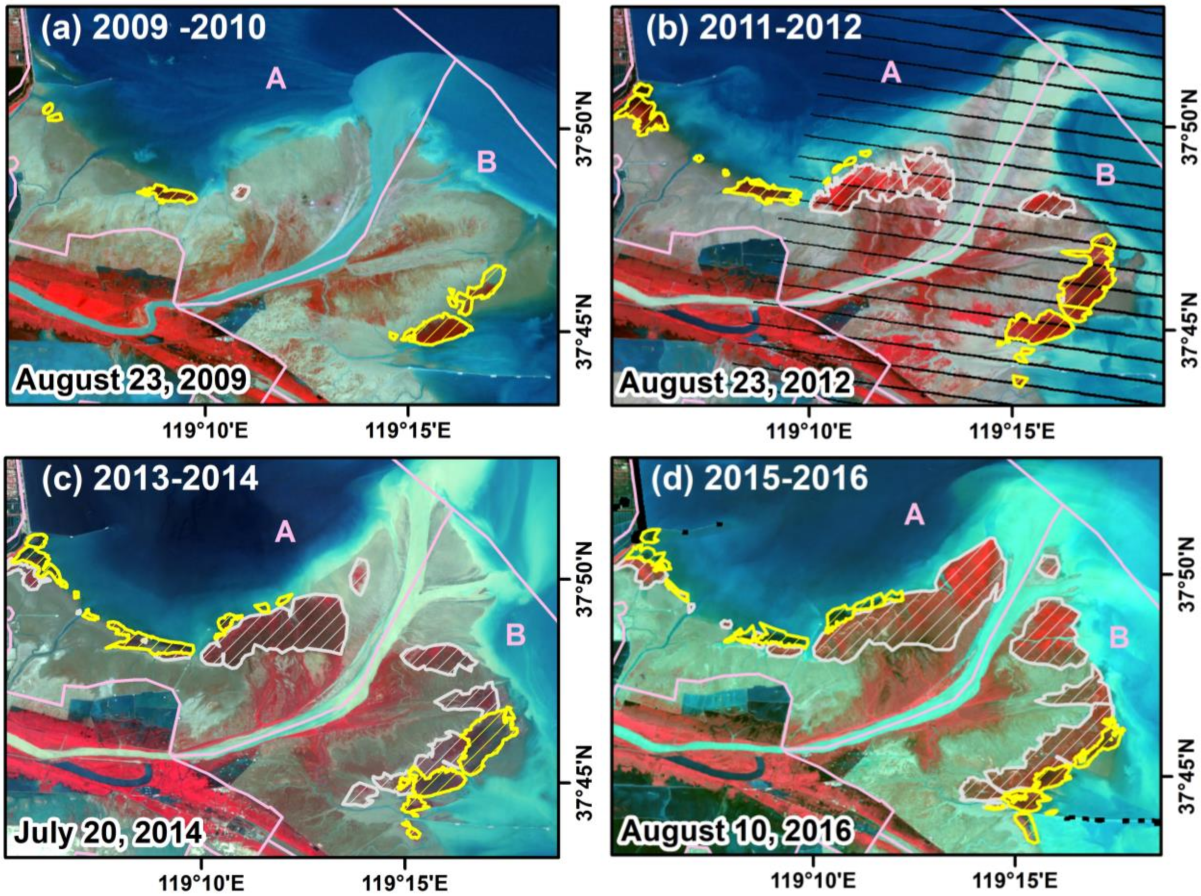

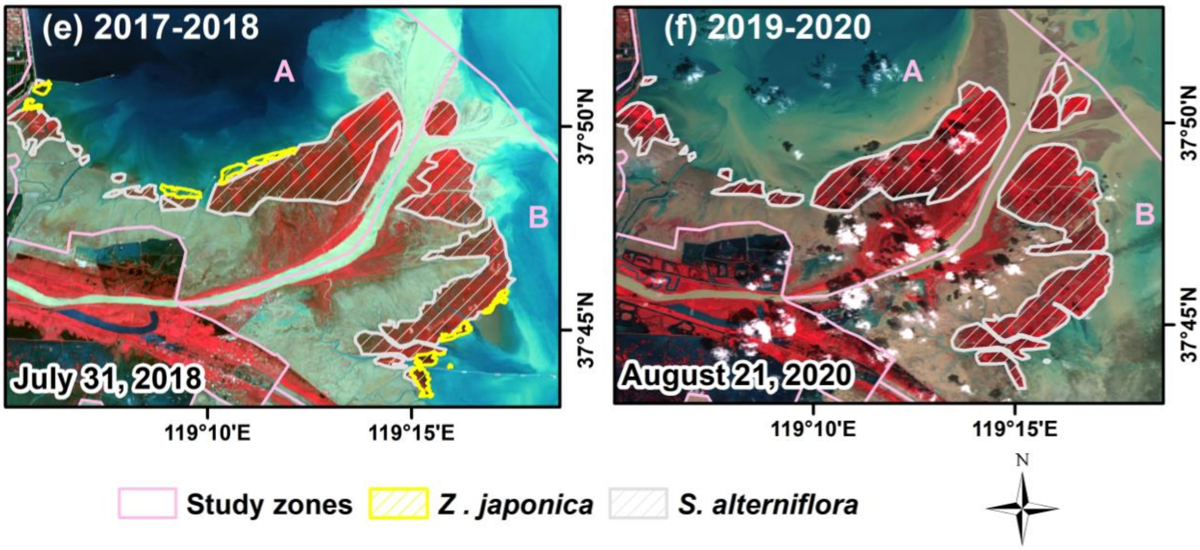

Fig. 12. Spatial distribution of *Z. japonica* and *S. alterniflora* in YRD from 2009 to 2020. Note that no *Z. japonica* was detected in 2019-2020.

5 Discussion

5.1 Advantages of SGI in seagrass mapping

In this study, we constructed SGI by taking into account both spectral, phenological and spatial characteristics of *Z. japonica* seagrass beds. Using SGI, we generated the first maps of *Z. japonica* seagrass beds from 1985 to 2018 in YRD. The resultant seagrass bed maps demonstrate good accuracies, with producer's accuracies higher than 90.06% and user's accuracies higher than 94.67%. The successful mapping can be explained by three advantages of SGI.

First, SGI was constructed by temporal composite approach on a pixel-by-pixel basis, which effectively alleviates the influence of frequent cloud cover and tidal inundations in coastal areas. Especially for seagrass beds that are submerged at high tide and exposed at low tide, the maximum NDVI composite image (i.e., $NDVI_{max}$) highlights the greenest growth condition of each *Z. japonica* pixel and eliminates the possible influence of tidal inundation on a single image. In recent years, the pixel-based approach has been increasingly utilized for coastal wetlands mapping and proved to achieve better accuracy than those from a single or multiple cloudless images because it allows all pixels with valid observations to be utilized regardless of the cloud coverage at a scene (Zhang et al., 2020; Jia et al., 2021; Hu et al., 2021; Sun et al., 2021; Xu et al., 2021). For example, Jia et al., (2021) proposed to use maximum mNDWI (mNDWI-MSIC) and maximum NDVI image composites (NDVI-MSIC) to extract tidal flat, with the former extracting coastline at high tidal level and the latter extracting coastline at low tidal level. Note that in our study, we used the minimum mNDWI composite to obtain the coastline at low tidal level instead of NDVI-MSIC. This is because the coastal water in YRD is highly turbid. For the water area in YRD, the NDVI-MSIC composite generates the most turbid pixels throughout a year, which are difficult to be distinguished from tidal flats as they have similar NDVI values. In contrast, mNDWI was less influenced by water turbidity (Xu, 2005). The minimum mNDWI of tidal flat pixels represents the status when they are fully exposed at low tide level, and thus help extract more accurate coastlines at low tide level.

Second, SGI considers the spectral and phenological characteristics, and spatial location of *Z. japonica* seagrass beds as well as salt marsh vegetations such as *S. alterniflora* and *S. salsa*. With *S. alterniflora* invading seaward, its niche overlaps with that of *Z. japonica* (Fig. 11). It is difficult to distinguish *S. alterniflora* and *Z. japonica* solely based on $NDVI_{max}$ (Fig. 5a). However, *S. alterniflora* is distributed in higher intertidal area and has much taller and dense plants compared to *Z. japonica*, thus its mNDWI at low tide level is negative and similar as terrestrial vegetation. As *Z. japonica* has short plants and is frequently submerged at high tide level, it has low brightness value than *S. salsa* and tidal flats. In addition, *Z. japonica* has much shorter growing length than salt marsh vegetation. Compared to any of the vegetation indices, the integration of spectral and phenological indices in SGI exaggerate the difference between *Z. japonica* and others.

Third, SGI allows automatic and rapid mapping of *Z. japonica* using unsupervised classification algorithm. As *Z. japonica* and other types showed distinct SGI values, the unsupervised extraction using multi-class Otsu algorithm achieved good accuracy. Most previous studies utilized supervised classification algorithms for seagrass mapping (Coffer et al., 2020; Kuhwald et al., 2021; Fernandes et al., 2022; Lebrasse et al., 2022). Sample collection is the most time-consuming and labor-intensive task in supervised classifications. It is especially difficult for the coastal wetlands as many areas are hard to reach for field surveyors. In addition, the long-term distribution of seagrass beds is usually poorly documented, hampering collection of sufficient training datasets for retrospective mapping. Compared to the supervised classification method, the unsupervised Otsu threshold segmentation algorithm does not require the collection of training samples and the classification process is automated without human intervention, which is suitable for the long time series and large-scale dynamic monitoring of seagrass beds in YRD. Therefore, SGI combined the multi-Otsu algorithm can be easily applied to other time-series satellite imagery such as Sentinel-2 or the Harmonized Landsat-8 Sentinel-2 surface reflectance for seagrass extraction. In 2021, Shandong Province started to implement seagrass beds restoration in the south of YRD. Our proposed method has potential to provide technical support and basic data for regular seagrass restoration monitoring.

5.2 Uncertainties and limitations of our seagrass mapping method

Although our method achieved high accuracy in long-term seagrass mapping YRD, uncertainties and limitations still exist. First, successful application of this method relied on temporally dense observations during specified phenological periods. Due to limited Landsat data before 1999 and scan-off failure in Landsat 7 ETM+ after 2003, our method generated seagrass bed maps every two years instead of performing annual mapping. Although using Landsat imagery during two-year period effectively increases the number of valid observations at pixel level and can better represent vegetation phenology, it may not capture the rapid annual change in *Z. japonica* seagrass beds. For example, research has shown that *S. alterniflora* can push over 10 m into *Z. japonica* region during several months (Yue et al., 2021). Because *S. alterniflora* has generally higher NDVI than *Z. japonica*, using $NDVI_{max}$ during two-year period probably identified *S. alterniflora* instead of *Z. japonica* for those pixels where *Z. japonica* was replaced by *S. alterniflora*. In this case, the seagrass bed maps represent the minimum area of *Z. japonica* during the two-year period. Nevertheless, the problem can be well resolved when dense observations are available during a year. Second, our method is suitable for intertidal seagrass extraction where the seagrass beds are exposed at low tide. For submerged seagrass beds in subtidal area, it may not work as water column correction is needed to retrieve correct bottom reflectance. Third, the 30 m-resolution Landsat images inevitably produce mixed-pixel problem. Small patches of *Z. japonica* seagrass beds with low biomass may not be identified. In July 2019, we found some small patches of *Z. japonica* in our field investigation in Zone B. Unfortunately, our method did not detect any of *Z. japonica* in this year.

5.3 Driving factors for *Z. japonica* seagrass beds variations in YRD

Previous studies have reported that many factors can cause the degradation and loss of seagrass beds, including coastal erosion, extreme climate events, and human activities such as coastal development and water pollutions (Kim et al., 2015; Kendrick et al., 2019; Oprandi et al., 2020). The YRD is probably one of the most active deltas in the world's estuaries because of large interannual and intra-annual variations in sediment transport and recent invasions of *S. alterniflora*. In YRD, the large variations of the spatial extents of *Z. japonica* during 1985-2018 (Fig. 9 and Fig. 10) indicates that the driving factors can be very complex. To date, no previous study has investigated the driving factors for the long-term spatial variations of *Z. japonica* meadows in YRD. Our results demonstrated two convincing factors for the loss of *Z. japonica* seagrass beds: (1) rapid and large amount of sediment deposition in the estuary due to river channel diversion and early implementation of WSRS, and (2) *S. alterniflora* invasion in the recent decade.

After each river channel diversion (1996 and 2007) and during the early stage of WSRS (2003-2006), the morphology of estuarine land changed substantially owing to rapid sediment deposition in the river mouth. Several patches were buried by the newly formed land, and the sediment burial hampers the germination of seeds (Cabaço and Santos, 2007), which could cause rapid loss of the patches (e.g., the patches in Zone B in 1996-1998 and Zone A in 2005-2006, Fig. 11f and Fig. 11j). Meanwhile, new seagrass patches started to grow in the newly formed intertidal area (e.g., the patches in Zone A in 2001-2002, Fig. 11h). Note that after 2007, the continuous implementation of WSRS seemed not affect seagrass beds, regardless of the highly turbid water around coastal area (Li et al., 2019). From 2007 to 2012 (before explosion of *S. alterniflora*), we did not observe rapid declination of *Z. japonica* area. This is consistent with recent in-situ field investigations and laboratory experiment by Hou et al. (2020) and Zhang et al. (2021), which concluded that *Z. japonica* in YRD shows good short-term resistance to high turbidity during WSRS.

S. alterniflora invasion is the primary reason for the gradual *Z. japonica*'s degradation in the recent decade. *S. alterniflora* has great reproduction capacity with both sexual and asexual reproduction. Our results showed that from 2013 to 2018, the area of *Z. japonica* has been encroached by *S. alterniflora* with 868.4 ha. Ma et al., (2020) reported that *S. alterniflora*, regardless of the plant densities, have significant inhibition effects on the symbiotic *Z. japonica*. The stem density, height and total biomass of *Z. japonica* decreased dramatically once the invading patches of *S. alterniflora* arise. Yue et al., (2021) explained three steps of *S. alterniflora* invading Z. japonica: first, seeds of *S. alterniflora* float into the *Z. japonica* and the sparse patches of the invader grow; subsequently, sediment accumulation increased with the growing density of clonal ramets, and the taller *S. alterniflora* patches blocked the sunlight needed for *Z. japonica*, gradually inhibiting the growth of *Z. japonica*; finally, the patches of *S. alterniflora* connected and replace the *Z. japonica* community.

Other possible factors that affect the growth of *Z. japonica* seagrass beds in YRD include soil erosion in local area and extreme climate events including drought and typhoon (timeline illustrated in Fig. 9). The loss in the *Z. japonica* patch near Gudong Oil field from 1985 may be explained by severe coastal erosion in this area. Ji et al., (2018) reported that Gudong nearshore experienced severe erosion (−0.1 m/yr) due to reduction of sediment supply and strong wave currents. In 2000-2002, the rapid loss of *Z. japonica* may be explained by severe drought events in 2000, typhoon Toraji in summer 2001 and typhoon Fengshen in summer 2002. The severe drought in Shandong Province in 2000 resulted in hyper-salinity and water column stratification in coastal YRD (Xi et al., 2001; Hall et al., 2016), which can lead to mortality of *Z. japonica*. Typhoon can be another factor. Recent investigations found that the super typhoon Lekima in 2019 resulted in over 100-fold loss of the area of *Z. japonica* in YRD due to strong winds, heavy rainfall and sudden soil erosion (Yue et al., 2021).

5.4 Implications for seagrass management and restoration

This study provides the first long-term *Z. japonica* seagrass bed maps in YRD, filling the knowledge gaps on the seagrass bed extents in coastal China. We hope our results can significantly facilitate in-depth understanding on the mechanisms and driving factors for *Z. japonica* variations in YRD, as well as the understanding on the ecosystem services they provide. It is unfortunate that the typhoon Lekima led to severe loss of *Z. japonica* meadows in YRD in 2019 (Yue et al., 2021). Restoration efforts are required urgently for seagrass meadow recovery. Our long-term *Z. japonica* seagrass maps can serve as an intrinsic basis for the development of seagrass restoration measures. In fact, in recent years numerous restoration efforts have been implemented in the coastal provinces in China, including Hebei, Shandong, Guangxi and Hainan provinces (Liu et al., 2016; Yu et al., 2019; Xiao et al., 2020). The long-term seagrass mapping methods developed in this study have great potential to be applied for timely monitoring and evaluation of the effectiveness of the restoration efforts at regional scale. As seagrass bed is one of the most important blue carbon ecosystems, our study provides baseline efforts for seagrass carbon storage estimation and long-term monitoring, which is critical to maintain coastal sustainability.

6 Conclusion

This paper proposed a new seagrass index, namely SGI, for automatic mapping of *Z. japonica*, an intertidal seagrass species widely distributed in China. SGI alleviates the influence of tidal inundation and enhances the spectral and phenological separability between seagrass beds and other cover types by incorporating temporal composites of NDVI, mNDWI and TCBI based on time-series remote sensing imagery. Using SGI, we then extracted *Z. japonica* extents in YRD based on all available Landsat 5/7/8 images during 1985-2018 with SGI thresholds automatically determined by multi-Otsu algorithm. The results showed that SGI has successfully discriminated the *Z. japonica* seagrass beds and non-*Z. japonica* types such as salt marshes, tidal flat and water. The SGI thresholds were relatively stable, ranging from 2.22 to 4.11. The overall accuracies were greater than 95%, producer's accuracies and user's accuracies of *Z. japonica* were greater than 90% and 94%, respectively, which were validated through field inventory data, high resolution satellite imagery and Landsat imagery. From 1985 to 2018, the area and spatial distribution of Z. japonica showed large variations (from 149 ha in 2005-2006 to 1302.9 ha in 2011-2012). River channel shifts in YRD altered the spatial distribution of *Z. japonica*, and the expansion of invasive salt marsh vegetation *S. alterniflora* caused gradual degradation of *Z. japonica* in recent years. Coastal erosion and extreme climate events such as drought and typhoon are other possible factors explaining Z. japonica area decline. In sum, this paper provides the first long-term seagrass bed maps in YRD. We expect that the SGI will advance automatic and rapid mapping methods for intertidal seagrass beds, and the *Z. japonica* maps will provide a baseline data for restoration and management of seagrasses at regional scale.

Acknowledgements

This research was supported by the National Natural Science Foundation of China (No. 42071396), and Beijing Science and Technology Planning Project (No. Z201100006720001), and Capacity Building for Sci-Tech Innovation—Fundamental Scientific Research Funds.

References

Adams, M., Hovey, R., Hipsey, M., Bruce, L., Ghisalberti, M., Lowe, R., Gruber, R., Ruiz-Montoya, L., Maxwell, P., Callaghan, D., Kendrick, G. and Brien, K., 2016. Feedback between sediment and light for seagrass: Where is it important? Limnol Oceanogr, 61: 1937-1955. https://doi.org/10.1002/lno.10319

Barrell, J. and Grant, J., 2015. High-resolution, low-altitude aerial photography in physical geography. Progress in Physical Geography: Earth and Environment, 39(4): 440-459. https://doi.org/10.1177/0309133315578943

Cabaço, S. and Santos, R., 2007. Effects of burial and erosion on the seagrass Zostera noltii. J Exp Mar Biol Ecol, 340(2): 204-212. https://doi.org/10.1016/j.jembe.2006.09.003

Calleja, F., Galván, C., Silió-Calzada, A., Juanes, J.A. and Ondiviela, B., 2017. Long-term analysis of Zostera noltei: A retrospective approach for understanding seagrasses' dynamics. Mar Environ Res, 130: 93-105. https://doi.org/10.1016/j.marenvres.2017.07.017

Campbell, A.D., Fatoyinbo, T., Charles, S.P., Bourgeau-Chavez, L.L., Goes, J., Gomes, H., Halabisky, M., Holmquist, J., Lohrenz, S., Mitchell, C., Moskal, L.M., Poulter, B., Qiu, H., Resende De Sousa, C.H., Sayers, M., Simard, M., Stewart, A.J., Singh, D., Trettin, C., Wu, J., Zhang, X., Lagomasino, D. and Oak Ridge National Lab. ORNL, O.R.T.U., 2022. A review of carbon monitoring in wet carbon systems using remote sensing. Environ Res Lett, 17(2): 025009. https://iopscience.iop.org/article/10.1088/1748-9326/ac4d4d

Carpenter, S., Byfield, V., Felgate, S.L., Price, D.M., Andrade, V., Cobb, E., Strong, J., Lichtschlag, A., Brittain, H., Barry, C., Fitch, A., Young, A., Sanders, R. and Evans, C., 2022. Using Unoccupied Aerial Vehicles (UAVs) to Map Seagrass Cover from Sentinel-2 Imagery. Remote Sens-Basel, 14(3): 477. https://doi.org/10.3390/rs14030477

Coffer, M.M., Schaeffer, B.A., Zimmerman, R.C., Hill, V., Li, J., Islam, K.A. and Whitman, P.J., 2020. Performance across WorldView-2 and RapidEye for reproducible seagrass mapping. Remote Sens Environ, 250: 112036. https://doi.org/10.1016/j.rse.2020.112036

Fan, Y., Chen, S., Zhao, B., Pan, S., Jiang, C. and Ji, H., 2018. Shoreline dynamics of the active Yellow River delta since the implementation of Water-Sediment Regulation Scheme: A remote-sensing and statistics-based approach. Estuar Coast Shelf S, 200: 406-419. https://doi.org/10.1016/j.ecss.2017.11.035

Fernandes, M.B., Hennessy, A., Law, W.B., Daly, R., Gaylard, S., Lewis, M. and Clarke, K., 2022. Landsat historical records reveal large-scale dynamics and enduring recovery of seagrasses in an impacted seascape. Sci Total Environ, 813: 152646. https://doi.org/10.1016/j.scitotenv.2021.152646

Fourqurean, J.W., Duarte, C.M., Kennedy, H., Marbà, N., Holmer, M., Mateo, M.A., Apostolaki, E.T., Kendrick, G.A., Krause-Jensen, D., McGlathery, K.J. and Serrano, O., 2012. Seagrass ecosystems as a globally significant carbon stock. Nat Geosci, 5(7): 505-509. https://doi.org/10.1038/ngeo1477

Green, A.E., Unsworth, R., Chadwick, M.A. and Jones, P., 2021. Historical Analysis Exposes Catastrophic Seagrass Loss for the United Kingdom. Front Plant Sci, 12: 629962. https://doi.org/10.3389/fpls.2021.629962

Hall, M.O., Furman, B.T., Merello, M. and Durako, M.J., 2016. Recurrence of Thalassia testudinum seagrass die-off in Florida Bay, USA: initial observations. Mar Ecol Prog Ser, 560: 243-249. https://doi.org/10.3354/meps11923

Hossain, M.S., Bujang, J.S., Zakaria, M.H. and Hashim, M., 2015. The application of remote sensing to seagrass ecosystems: an overview and future research prospects. Int J Remote Sens, 36(1): 61-114. https://doi.org/10.1080/01431161.2014.990649

Hossain, M.S., Bujang, J.S., Zakaria, M.H. and Hashim, M., 2015b. The application of remote sensing to seagrass ecosystems: an overview and future research prospects. Int J Remote Sens, 36(1): 61-114. https://doi.org/10.1080/01431161.2014.990649

Hou, C., Song, J., Yan, J., Wang, K., Li, C. and Yi, Y., 2020. Growth indicator response of Zostera japonica under different salinity and turbidity stresses in the Yellow River Estuary, China. Mar Geol, 424: 106169. https://doi.org/10.1016/j.margeo.2020.106169

Hu, Y., Tian, B., Yuan, L., Li, X., Huang, Y., Shi, R., Jiang, X., Wang, L. and Sun, C., 2021. Mapping coastal salt marshes in China using time series of Sentinel-1 SAR. Isprs J Photogramm, 173: 122-134. https://doi.org/10.1016/j.isprsjprs.2021.01.003

Iacarella, J., Adamczyk, E., Bowen, D., Chalifour, L., Eger, A., Heath, W., Helms, S., Hessing-Lewis, M., Hunt, B., MacInnis, A., O'Connor, M., Robinson, C., Yakimishyn, J. and Baum, J., 2018. Anthropogenic disturbance homogenizes seagrass fish communities. Global Change Biol, 24. https://doi.org/10.1111/gcb.14090

Ji, H., Chen, S., Pan, S., Xu, C., Jiang, C. and Fan, Y., 2018. Morphological variability of the active Yellow River mouth under the new regime of riverine delivery. J Hydrol, 564: 329-341. https://doi.org/10.1016/j.jhydrol.2018.07.014

Jia, M., Wang, Z., Mao, D., Ren, C., Wang, C. and Wang, Y., 2021. Rapid, robust, and automated mapping of tidal flats in China using time series Sentinel-2 images and Google Earth Engine. Remote Sens Environ, 255: 112285.

Kauth, R.J.A.T., 1976. The Tasselled Cap -A Graphic Description of the Spectral-Temporal Development of Agricultural Crops as Seen by LANDSAT. LARS Symposia: 159. https://docs.lib.purdue.edu/lars_symp/159/

Kendrick, G.A., Nowicki, R.J., Olsen, Y.S., Strydom, S., Fraser, M.W., Sinclair, E.A., Statton, J., Hovey, R.K., Thomson, J.A., Burkholder, D.A., McMahon, K.M., Kilminster, K., Hetzel, Y., Fourqurean, J.W., Heithaus, M.R. and Orth, R.J., 2019. A Systematic Review of How Multiple Stressors From an Extreme Event Drove Ecosystem-Wide Loss of Resilience in an Iconic Seagrass Community. Front Mar Sci, 6.

https://doi.org/10.3389/fmars.2019.00455

Kim, K., Choi, J., Ryu, J., Jeong, H.J., Lee, K., Park, M.G. and Kim, K.Y., 2015. Observation of typhoon-induced seagrass die-off using remote sensing. Estuar Coast Shelf S, 154: 111-121. https://doi.org/10.1016/j.ecss.2014.12.036

Kuhwald, K., Schneider Von Deimling, J., Schubert, P., Oppelt, N., Scales, K. and Lecours, V., 2021. How can Sentinel‐2 contribute to seagrass mapping in shallow, turbid Baltic Sea waters? Remote Sens Ecol Con. https://doi.org/10.1002/rse2.246

Lebrasse, M.C., Schaeffer, B.A., Coffer, M.M., Whitman, P.J., Zimmerman, R.C., Hill, V.J., Islam, K.A., Li, J. and Osburn, C.L., 2022. Temporal Stability of Seagrass Extent, Leaf Area, and Carbon Storage in St. Joseph Bay, Florida: a Semi-automated Remote Sensing Analysis. Estuar Coast. https://link.springer.com/article/10.1007/s12237-022-01050-4

Li, P., Ke, Y., Bai, J., Zhang, S., Chen, M. and Zhou, D., 2019. Spatiotemporal dynamics of suspended particulate matter in the Yellow River Estuary, China during the past two decades based on time-series Landsat and Sentinel-2 data. Mar Pollut Bull, 149: 110518. https://doi.org/10.1016/j.marpolbul.2019.110518

Li, P., Ke, Y., Wang, D., Ji, H., Chen, S., Chen, M., Lyu, M. and Zhou, D., 2021. Human impact on suspended particulate matter in the Yellow River Estuary, China: Evidence from remote sensing data fusion using an improved spatiotemporal fusion method. Sci Total Environ, 750: 141612. https://doi.org/10.1016/j.scitotenv.2020.141612

Li, Y., Bai, J., Zhang, L. and Li, T., 2021. Review on the research of seagrass optical remote sensing monitoring. Journal of Tropical Oceanography, 40(6): 1-13.

DOI:10.11978/2020110

Li, Y., Du, Z., Wang, X., Yang, Q., Chen, Z., Sun, Y. and Liu, D., 2019. Evaluation of wetland ecosystem services in Yellow River Delta Nature Reserve. Marine Environmental Science, 38(5): 761-768. DOI: 10.13634/j.cnki.mes.2019.05.017

Liao, P.S., Chew, T.S. and Chung, P.C., 2001. A fast algorithm for multilevel thresholding. J Inf Sci Eng, 17(5): 713-727.

Liu, P., Zhang, H., Chen, L. and Sun, Y., 2019. Rhizosphere microbial community structure and function of Zostera japonica in the distribution area of seagrass beds in the Yellow Sea and Bohai Sea. Acta Microbiologica Sinica, 59(08): 1484-1499. DOI: 10.13343/j.cnki.wsxb.20180432

Liu, Z., Cui, B. and He, Q., 2016. Shifting paradigms in coastal restoration: Six decades' lessons from China. Sci Total Environ, 566-567: 205-214. https://doi.org/10.1016/j.scitotenv.2016.05.049

Ludwig, C., Walli, A., Schleicher, C., Weichselbaum, J. and Riffler, M., 2019. A highly automated algorithm for wetland detection using multi-temporal optical satellite data. Remote Sens Environ, 224: 333-351. https://doi.org/10.1016/j.rse.2019.01.017

Ma, X., Wang, A., Fu, S., Yue, X. and Dongdong, Q., 2020. Ecological effects of invasive species Spartina alterniflora on Zostera japonica in the Yellow River Delta. Environmental Ecology, 2(04): 65-71.

Oprandi, A., Mucerino, L., De Leo, F., Bianchi, C.N., Morri, C., Azzola, A., Benelli, F., Besio, G., Ferrari, M. and Montefalcone, M., 2020. Effects of a severe storm on seagrass meadows.

Sci Total Environ, 748: 141373. https://doi.org/10.1016/j.scitotenv.2020.141373

Otsu, N., 1979. A threshold selection method from gray-level histograms. IEEE Transactions on Systems Man & Cybernetics, 9(1): 62-66.

Programme, U.N.E., 2020. Out of the Blue: The value of seagrasses to the environment and to people.

Ren, G., Wang, J., Wang, A., Wang, J., Zhu, Y., Wu, P., Ma, Y. and Zhang, J., 2019. Monitoring the Invasion of Smooth Cordgrass Spartina alterniflora within the Modern Yellow River Delta Using Remote Sensing. J Coastal Res: 135-145. https://doi.org/10.2112/SI90-017.1

Salinas, C., Duarte, C.M., Lavery, P.S., Masque, P., Arias Ortiz, A., Leon, J.X., Callaghan, D., Kendrick, G.A. and Serrano, O., 2020. Seagrass losses since mid‐20th century fuelled CO_2 emissions from soil carbon stocks. Global Change Biol, 26(9): 4772-4784. https://doi.org/10.1111/gcb.15204

Singh, K.V., Setia, R., Sahoo, S., Prasad, A. and Pateriya, B., 2015. Evaluation of NDWI and MNDWI for assessment of waterlogging by integrating digital elevation model and groundwater level. Geocarto Int, 30(6): 650-661. https://doi.org/10.1080/10106049.2014.965757

Somers, B., Delalieux, S., Verstraeten, W.W., Van Aardt, J., Albrigo, G.L. and Coppin, P., 2010. An automated waveband selection technique for optimized hyperspectral mixture analysis. Int J Remote Sens, 31(20): 5549-5568. https://doi.org/10.1080/01431160903311305

St-Pierre, A.P. and Gagnon, P., 2020. Kelp-bed dynamics across scales: Enhancing mapping capability with remote sensing and GIS. J Exp Mar Biol Ecol, 522: 151246. https://doi.org/10.1016/j.jembe.2019.151246

Sun, C., Li, J., Liu, Y., Liu, Y. and Liu, R., 2021. Plant species classification in salt marshes using phenological parameters derived from Sentinel-2 pixel-differential time-series. Remote Sens Environ, 256: 112320. https://doi.org/10.1016/j.rse.2021.112320

Tu, N.H.C., Uyen, N.T., Doc, L.Q., Tuan, L.C., Thu, M.A. and Tin, H.C., 2021. Impacts of urbanization and land transitions on seagrass beds in tropical lagoon in central Vietnam. Reg Stud Mar Sci, 45: 101860. https://doi.org/10.1016/j.rsma.2021.101860

Valle, M., Palà, V., Lafon, V., Dehouck, A., Garmendia, J.M., Borja, Á. and Chust, G., 2015. Mapping estuarine habitats using airborne hyperspectral imagery, with special focus on seagrass meadows. Estuar Coast Shelf S, 164: 433-442. https://doi.org/10.1016/j.ecss.2015.07.034

Veettil, B.K., Ward, R.D., Lima, M.D.A.C., Stankovic, M., Pham, N.H. and Ngo, X.Q., 2020. Opportunities for seagrass research derived from remote sensing: A review of current methods. Ecol Indic, 117. https://doi.org/10.1016/j.ecolind.2020.106560

Wang, Z., Ke, Y., Chen, M., Zhou, D., Zhu, L. and Bai, J., 2021. Mapping coastal wetlands in the Yellow River Delta, China during 2008–2019: impacts of valid observations, harmonic regression, and critical months. Int J Remote Sens, 42(20): 7880-7906. https://doi.org/10.1080/01431161.2021.1966852

Xi, X., Zheng, S. and Tang, Z., 2001. Analysis and Countermeasures of spring and summer drought in Shandong Peninsula in 2000. Shandong Meteorology(02): 9-11. DOI：

10.19513/j.cnki.issn1005-0582.2001.02.004

Xiao, X., Huang, Y. and Holmer, M., 2020. Current trends in seagrass research in China (2010-2019). Aquat Bot, 166: 103266. https://doi.org/10.1016/j.aquabot.2020.103266

Xu, H., 2005. A Study on Information Extraction of Water Body with the Modified Normalized Difference Water Index (MNDWI). JOURNAL OF REMOTE SENSING(05): 589-595.

Xu, R., Zhao, S. and Ke, Y., 2021. A Simple Phenology-Based Vegetation Index for Mapping Invasive Spartina Alterniflora Using Google Earth Engine. Ieee J-Stars, 14: 190-201. Doi: 10.1109/JSTARS.2020.3038648.

Xu, S., Xu, S., Zhou, Y., Yue, S., Zhang, X., Gu, R., Zhang, Y., Qiao, Y. and Liu, M., 2021. Long-Term Changes in the Unique and Largest Seagrass Meadows in the Bohai Sea (China) Using Satellite (1974–2019) and Sonar Data: Implication for Conservation and Restoration. Remote Sens-Basel, 13(5): 856. https://doi.org/10.3390/rs13050856

Yang, Z., Ji, Y., Bi, N., Lei, K. and Wang, H., 2011. Sediment transport off the Huanghe (Yellow River) delta and in the adjacent Bohai Sea in winter and seasonal comparison. Estuar Coast Shelf S, 93(3): 173-181. https://doi.org/10.1016/j.ecss.2010.06.005

Yu, S., Zhang, J., Cui, L., Jiang, Z., Zhang, L. and Huang, X., 2019. Preliminary study on seed-based restoration for Enhalus acoroides meadow. J. Trop. Oceanog., 38: 49-54.

Yue, S., Zhang, X., Xu, S., Liu, M., Qiao, Y., Zhang, Y., Liang, J., Wang, A. and Zhou, Y., 2021. The super typhoon Lekima (2019) resulted in massive losses in large seagrass (Zostera japonica) meadows, soil organic carbon and nitrogen pools in the intertidal Yellow River Delta, China. Sci Total Environ, 793: 148398.

https://doi.org/10.1016/j.scitotenv.2021.148398

Yue, S., Zhou, Y., Xu, S., Zhang, X., Liu, M., Qiao, Y., Gu, R., Xu, S. and Zhang, Y., 2021. Can the Non-native Salt Marsh Halophyte Spartina alterniflora Threaten Native Seagrass (Zostera japonica) Habitats? A Case Study in the Yellow River Delta, China. Front Plant Sci, 12. https://doi.org/10.3389/fpls.2021.643425

Zhang, J., Wang, K., Yi, Q., Pei, Y., Hou, C. and Yi, Y., 2021. Growth of Zostera japonica in different sediment habitats of the Yellow River estuary in China. Environ Sci Pollut R, 28(24): 31151-31162. DOI:10.1007/s11356-021-12925-7

Zhang, X., Lin, H., Song, X., Xu, S., Yue, S., Gu, R., Xu, S., Zhu, S., Zhao, Y., Zhang, S., Han, G., Wang, A., Sun, T. and Zhou, Y., 2019. A unique meadow of the marine angiosperm Zostera japonica, covering a large area in the turbid intertidal Yellow River Delta, China. Sci Total Environ, 686: 118-130. https://doi.org/10.1016/j.scitotenv.2019.05.320

Zhang, X., Xiao, X., Wang, X., Xu, X., Chen, B., Wang, J., Ma, J., Zhao, B. and Li, B., 2020. Quantifying expansion and removal of Spartina alterniflora on Chongming island, China, using time series Landsat images during 1995–2018. Remote Sens Environ, 247: 111916. https://doi.org/10.1016/j.rse.2020.111916

Zhou, Y., Zhang, X., Xu, S., Song, X., Lin, H., Wang, P. and Gu, R., 2016. New discovery of larger seagrass beds with areas > 50 ha in temperate waters of China: An unusual large seagrass (Zostera japonica) bed in the Yellow River estuary. Marine Sciences, 40(09): 95-97.

Zoffoli, M.L., Gernez, P., Godet, L., Peters, S., Oiry, S. and Barillé, L., 2021. Decadal increase in the ecological status of a North-Atlantic intertidal seagrass meadow observed with multi-mission satellite time-series. Ecol Indic, 130: 108033. https://doi.org/10.1016/j.ecolind.2021.108033

Zoffoli, M.L., Gernez, P., Rosa, P., Le Bris, A., Brando, V.E., Barillé, A., Harin, N., Peters, S., Poser, K., Spaias, L., Peralta, G. and Barillé, L., 2020. Sentinel-2 remote sensing of Zostera noltei-dominated intertidal seagrass meadows. Remote Sens Environ, 251: 112020. https://doi.org/10.1016/j.rse.2020.112020